B,5
P-88

MCR-73-12

ABLATIVE AND METALLIC HEAT SHIELDS

FOR AEROBRAKING REENTRY

TASK B-3 REPORT

January, 1973

(NASA-CR-185905) ABLATIVE AND METALLIC HEAT SHIELDS FOR AEROBRAKING REENTRY, TASK B-3 REPORT (Martin Marietta Aerospace) 88 p

N90-70124

Unclas

00/18 0234034

Contract NAS8-27161

MARTIN MARIETTA AEROSPACE
Denver Division
P. O. Box 179
Denver, Colorado 80201

#234034

MCR-73-12

Ablative and Metallic Heat Shields for Aerobraking Reentry

Task B-3 Report

January, 1973

Contract NAS8-27161

Approved by:

Eric L. Strauss

Eric L. Strauss
Program Manager

MARTIN MARIETTA AEROSPACE
Denver Division
P. O. Box 179
Denver, Colorado 80201

FOREWORD

This report is submitted in compliance with Phase II, Task 5 (Reports) of Exhibit A, Scope of Work, dated 29 June 1972 for Contract NAS8-27161.

Phase II of the Contract consists of five Tasks:

Task I: Test Environment and Model Definition

Task II: Model Design and Fabrication

Task III: Ablator Test and Evaluation

Task IV: Conference Requirement

Task V: Reports

This report documents the studies performed under Task III: "Ablator Test and Evaluation."

TABLE OF CONTENT

LIST OF TABLES

LIST OF FIGURES

LIST OF FIGURES (Continued)

LIST OF FIGURES (Continued)

I. INTRODUCTION

The objectives of this study were to establish the feasibility of utilizing ablative or metallic heat shields for aerobraking reentry and to ascertain realistic ablative heat shield weights and design criteria for both ablative and metallic heat shields.

The ablative and metallic heat shields were for application to a 14 ft-diameter cylindrical body entry configuration with a 2:1 elliptical dome. Both a low drag and high drag configuration were studied. The high drag would be achieved by attachment of a 60° flare at the aft end of the cylinder. The aerobraking trajectory pertained to the transfer of the vehicle from a geosynchronous orbit to the orbit of the Space Shuttle. Aerobraking trajectories involving two perigee passes and 30 perigee passes were investigated.

In the performance of Task 3, "Ablator Test and Evaluation", the following was accomplished:

1. The plasma arc facility was calibrated for selected heat pulses with respect to cold wall heat flux to 2-1/2 and 8-in. diameter models, enthalpy and stagnation pressure.

2. Six 2-1/2 in.-diameter models were tested under conditions simulating "Two Pass" stagnation point heating for the low drag configuration (3 models) and the high drag configuration (3 models).

3. Six 8 in.-diameter models were tested under conditions simulating "Thirty Pass" stagnation point heating for the high drag configuration for all 30 entry passes (3 models) and for the first 15 entry passes (3 models).

4. Tested models were sectioned and photographed. Surface recession, char depth, pyrolysis depth and char stability were determined. Thermocouple and optical pyrometer data from the test runs was plotted and analyzed.

5. Selected ablator specimens were analyzed for test pulse heating and analyses were correlated with measured temperature and char depth data.

6. Total ablator weight was determined for the elliptical dome for both 2 pass and 30 pass entry heating.

7. Technological deficiencies of ablative heat shields for aerobraking reentry were ascertained.

The ablator models are described in the Task B-2 Report (MCR-73-2). The selected plasma arc test pulses are defined in the Task B-1 Report (MCR-72-324).

II. PLASMA ARC FACILITY AND CALIBRATION

Plasma arc tests were conducted in the Martin Marietta Corporation Facility B. It is powered by two direct current silicon rectifier systems capable of providing up to 1.5 megawatts of power to the arc generator. The facility B test chamber is a water-cooled double jacketed cylindrical tank, 48 in. in diameter and 12 ft long. It contains two viewing ports, located on either side along the horizontal centerline and slightly downstream from the nozzle exit plane. Additional ports for viewing the model front face with pyrometers or cameras are located in the end plate. The tank is slit along the top centerline and is flanged to support a second tank in piggyback fashion. The upper tank houses the model/instrument support and insertion mechanism. This mechanism contains three model holders, a calorimeter and a pitot probe. Each can be selectively inserted, traversed laterally and longitudinally, and retracted. It is operated from a remote control station. Tank vacuum is provided by a 3300 cfm mechanical pumping system and by a five stage steam ejector. A liquid oxygen and nitrogen station coupled with a high pressure vaporizer/compressor system provides gases for arc operation.

The arc generator is gas and magnetically stabilized Thermal Dynamics Corporation F-5000 unit. It consists of a water-cooled thoriated tungsten cathode and a cylindrical copper anode. Nitrogen is injected tangentially at the cathode. This initiates the vortex and shields the tungsten material against oxidation. Oxygen is injected into the anode in a quantity to yield the chemical equivalent of air. Oxygen is injected in a manner to increase the vortex strength and to mix efficiently with the nitrogen flow.

For testing 2-1/2 in.-diameter ablator models, a 3 in. exit diameter nozzle was used. This nozzle has an area ratio of 5.8 and operates at a nominal Mach number of 3.0. The 10 in. exit diameter nozzle used for testing the 8 in. diameter ablator models has an area ratio of 51.4 and operates at a nominal Mach number of 4.6.

Test points were calibrated by recording the arc current and voltage and the oxygen and nitrogen flow rates and by measuring cold wall heat flux, enthalpy and pitot pressure. Heating rates were measured with a calorimeter of the same diameter as the test model which contained a Gardon heat flux sensor at its center. Enthalpy was computed from a system energy balance. Calibration data are summarized in Table 1. The calibrated test points agree closely with the selected test conditions defined in Figures 31, 32, 35 and 36 of Reference 1.

III. TWO PASS ENTRY TESTING

Six plasma arc models, 2-1/2 in. in diameter, were tested for two pass heating. The test models are described in Table 1 and Figure 1 of Reference 2. The proposed test conditions are shown in Figures 31 and 32 of Reference 1. The actual heating rates, enthalpies and pressures attained in the tests are summarized in Table 2 and compared with flight conditions and proposed test plan conditions, in Table 3. Thermocouple output was continually recorded during the tests and during portions of the cool-down. In addition, surface temperature was measured with a recording optical pyrometer. Specimen response to the heat flux exposure was monitored with a motion picture camera at a one frame per second rate.

Time-temperature traces for thermocouples and optical pyrometers are shown in Figures 1 through 6. In a number of instances, instrumentation or equipment malfunction occurred and only partial temperature data were obtained. In general, the temperature data obtained were very satisfactory and duplicate specimens yielded similar temperature responses. Plasma arc models after test are shown in Figure 7. 3X enlarged views of the ablator front face are shown in Figures 8 through 13. With the exception of minor char loss at the model periphery, the models sustained no damage during the test. The model surface consists of a crusty silica layer.

IV. 30 AND 15-PASS ENTRY TESTING

Six plasma arc models, 8 in. in diameter, were tested for 30-pass heating (3 models) and 15-pass heating (3 models). The test models are described in Table 2 and Figure 9 of Reference 2. The proposed test conditions are shown in Figures 35 and 36 of Reference 1. The actual heating rates, enthalpies and pressures attained in the tests are summarized in Table 4. Peak values are compared with flight conditions and proposed test plan conditions in Table 3. Test procedures were similar to those employed for the 2-pass heating tests.

Time-temperature traces for thermocouples and optical pyrometers are shown for selected test pulses in Figures 14 and 15. Instrumentation or equipment malfunction occurred occasionally during the tests and resulted in only partial data acquisition for some runs. In general, the temperature data obtained were very good and duplicate specimens yielded similar temperature responses. Plasma arc models after testing are shown in Figure 16. Full size views of the ablator front face are shown in Figures 17 through 22. Localized char loss at the model periphery occurred in ESA-3560 models 1 and 2 (30-pass exposures). This char loss was due to the open honeycomb cells at the periphery which provided only partial support for the ablator char.

V. ABLATOR MODEL AND TEST DATA ANALYSIS

Tested models were sectioned to measure char depth and to characterize the nature of the char. Figures 23 through 26 show the cross-section of 2-1/2 in.-diameter models. Each model exhibits two distinct char cleavage planes parallel to the ablator surface. These planes represent the depth of char formation after the first and second heating pass respectively. The formation of a horizontal char cleavage plane is characteristic of silicone ablators. In addition, a series of vertical fissures is evident as a result of the shrinkage process which accompanies char formation. The severity of the vertical fissures increases with decreasing ablator density; i.e., the fissures are larger and more widespread in the ESA-3560 and SLA-561 ablators than in the ESA-5500 ablator. Cross-sections of 8 in.-diameter models are shown in Figures 27 through 30. The horizontal cleavage planes are also evident in the 30 and 15-pass models. However, the vertical char fissures are less pronounced in the 8-inch models than in the 2-1/2-inch models. This is because the lower heat flux experienced by the 8-inch models causes less severe char shrinkage.

Measured char depths are tabulated in Table 5. The transition from pyrolysis zone to virgin ablator is very gradual and cannot be pinpointed. Surface recession was also measured on the sectioned models and is listed in Table 5. Total ablator height increased in the ESA-5500 and ESA-3560 models due to the swelling action of the silicone resin during ablation. The SLA-561 ablator contains a lower concentration of silicone resin than the higher density ablators and silicone swelling is offset by contraction of the fillers during ablation, resulting in an overall reduction in ablator height.

Temperatures at the end of each heating pulse are presented graphically for 30-pass and 15-pass heating in Figures 31 through 36. The first two thermocouples (at nominal depths of 0.10 and 0.30 in.) show a steady increase in temperature for thirty-pass heating. The thermocouple at 0.65 in. starts to rise after the tenth pass. The thermocouple at 1.37 in. shows only a slight increase in temperature while the back wall thermocouple registers no temperature rise at end of heating throughout the thirty heating cycles. Differences in temperature response between duplicate specimens are due in part to differences in thermocouple locations.

VI. TEST DATA CORRELATION WITH ANALYSIS

The following specimens were analyzed for test pulse conditions:

ESA-5500; 2-Pass Heating; Low Drag Simulation

ESA-3560; 2-Pass Heating; High Drag Simulation

ESA-3560; 30-Pass Heating; High Drag Simulation

ESA-3560; 15-Pass Heating; High Drag Simulation

Calculated time-temperature plots for two-pass heating are shown in Figures 37 and 38. Time-temperature plots for 30-pass heating (Pass 30) and 15-pass heating (Pass 15) are shown in Figures 39 and 40 respectively. The calculated progression of char depth and pyrolysis zone during 30-pass and 15-pass heating is shown in Figure 41. Figures 42 and 43 show the analytically predicted temperatures for ESA-3560 models at the end of each heating pass for 30-pass and 15-pass heating respectively. The initial temperature was taken as 80°F for the first pulse and as 115°F for each subsequent pulse.

Table 5 lists the analytically predicted char thickness and pyrolysis depth and compares predicted and measured char depth. For the 8-inch models (30-pass and 15-pass heating), the correlation is excellent. For the 2-1/2-inch models (2-pass heating) the measured char thicknesses exceed calculated values by approximately 20 percent.

Table 6 compares analytically predicted and measured temperatures at the thermocouple depths for two-pass heating. The comparison is at the end of the first and second heating pulses and is tabulated as the difference between the final temperature and the temperature at the beginning of the heat pulse. The correlation is generally good within the ablator. On the aluminum backface, the analysis predicts no temperature rise or a very small rise at the end of the heat pulses. The measured temperature rise for the second heat pulse is 100° to 125°F.

Tables 7 and 8 compare analytically predicted and measured temperatures at the thermocouple depths for 30-pass heating and 15-pass heating respectively. The comparison is for passes 1, 5, 15, 25, 28 and 30 for 30-pass heating and for passes 1, 4, 6, 8, 12 and 15 for 15-pass heating. The data are tabulated as the difference between the temperature at the end of heating and the temperature at the beginning of the heat pulse. Measured surface temperatures were higher than the calculated values. Temperature correlation within the ablator and on the aluminum backface is satisfactory.

Table 9 lists the peak backwall temperature reached after the final test pulse in each of the models and compares the measured temperature rise (peak temperature minus temperature at start of the final heating pass) with the analytically predicted rise. In a number of instances, test data was not acquired and computer runs were not extended for a sufficiently long time period to obtain the temperature peak. In that case, the last measured or calculated temperature is listed in Table 9. As was the case for char depth, agreement is good for the 8-inch models while for the 2-1/2-inch models, the measured temperature rise is consistently higher than the calculated value.

The poor correlation for the 2-1/2-inch models is attributable to the specimen configuration. The assumption of one-dimensional heat flow, while it applies to the center of the 8-inch model, is not really valid for 1.36 in. and 2.03 in. high 2-1/2-in.-diameter models where the model center is only 1.25 inch from the periphery. In these models, backface temperatures are influenced by side heating. Since the desired 120 BTU/ft^2-sec heating rate could not be attained with models of greater than 2-1/2 in. diameter, this model size was selected even though it was recognized that the model height-to-diameter ratio was nonoptimum. The good agreement between measured and calculated temperatures in the ablator at end of heating (Table 6) verifies the analysis for two-pass entry heating.

VII. ABLATIVE HEAT SHIELD WEIGHTS

Ablative heat shield weights have been calculated for low drag and high drag configurations flying two-pass and 30-pass aerobraking trajectories and for different heat shield materials and material combinations. The surface area of the elliptical dome was calculated to be 30,694 $in.^2$. Figure 44 is a plot of dome area as a function of distance from the stagnation point (Semi Arc Length). The length of the semi-arc of the 2:1 elliptical dome with a 84-in. semi-major axis is 101.8 inch.

Ablator thickness requirements were determined as a function of dome location (semi-arc length). Required data were the "Heating Rate Distribution for a 2:1 Ellipse" (Figure 8 of Reference 1) and the "Ablator Design Curves for Two-Pass and 30-Pass Entry Missions" (Figures 45 and 46). Curves showing ablator thickness vs semi-arc length are presented in Figure 47. The reduced ablator thickness near the stagnation point is due to the greater mass of the aluminum backup structure at that location.

Figure 48, Ablator Thickness vs Dome Area, is constructed from Figure 47. The integrals (areas under the curves) for Figure 48 are the total ablator volumes in cubic inches. By converting the ablator volume to units of cubic feet and multiplying by the density in lb/ft^3, the total ablator weights are obtained. These ablator weights are tabulated in Table 10.

The heating rate across the elliptical dome varies from 100% to less than 10% of stagnation point heating. Therefore, the use of a single ablation material over the entire dome provides a nonoptimum design from the weight standpoint. The three ablation materials, ESA-5500 (55 lb/ft^3), ESA-3560 (30 lb/ft^3) and SLA-561 (15 lb/ft^3) use the same silicone resin system and are contained in the same honeycomb reinforcement core. They are therefore mutually compatible and can be used in combination. The following criteria are used for composite ablator designs:

ESA-5500 - $\dot{q} > 100$ BTU/ft^2-sec

ESA-3560 - $25 < \dot{q} < 100$ BTU/ft^2-sec

SLA-561 - $\dot{q} < 25$ BTU/ft^2-sec

The locations of ablator interfaces in composite designs are shown in Figures 47 and 48. The weight of composite designs are listed in Table 10.

For the 2-pass entry--low drag heating environment, an ESA-3560 ablative heat shield (weight = 713 lb) is the recommended design. Plasma arc testing has shown that ESA-3560 can withstand the 125 BTU/ft^2-sec peak heating rate at the stagnation point. An all ESA-3560 heat shield weighs only one-half as much as a composite ESA-5500/ESA-3560 heat shield.

For 2-pass--high drag heating, a composite ESA-3560/SLA-561 heat shield (weight = 622 lb) is the recommended design. The weight of an all ESA-3560 heat shield is 9% greater. An all SLA-561 heat shield (weight = 379 lb) is a potential candidate since plasma arc tests have shown that this material can withstand the heating environment. However, the weak char structure of SLA-561 requires further testing and evaluation to qualify the material for this mission.

A composite ESA-3560/SLA-561 heat shield (weight = 859 lb) is also the recommended design for the 30-pass-low drag mission. Similarly to the 2-pass-high drag mission, an all SLA-561 heat shield holds promise of meeting flight requirements with a large resultant weight saving.

For the 30-pass--high drag heating environment, an all SLA-561 heat shield (weight - 437 lb) is the recommended design. An ESA-3560 heat shield is more than twice as heavy.

VIII. TECHNOLOGICAL DEFICIENCIES

Two-pass and 30-pass plasma arc testing revealed that the ablators tested are capable of withstanding the aerobraking heating environment. Char loss only occurred at the periphery of the models where the honeycomb cells are cut. The char of all three ablators contained char fissures both parallel and perpendicular to the ablator surface. This is characteristic of silicone ablators and a fissure plane is always present at the interface between the char and the pyrolysis zone. The char is retained primarily by its adhesion to the honeycomb cell walls. The addition of glass or silica fibers of at least 1/4-in. length to the ablator provides a mechanism for bridging fissures. All three ablators contain fibers; however, for multipass heating, a higher fiber concentration may be preferred.

ESA-3560 and ESA-5500 ablators tend to swell during ablative degradation due to the swelling action of the silicone resin. SLA-561, on the other hand, contains a much lower percentage of silicone resin in relationship to fillers and the swelling tendency of the resin is counteracted by the shrinkage of the fillers during ablation such that the net effect is one of char shrinkage. A silicone ablator intermediate in density and resin content between ESA-3560 and SLA-561 could be formulated such that no volumetric change occurs during char formation. Such an ablator would be optimum from a char stability standpoint for multipass thermal protection.

Thermal and ablative properties of all three ablators are well characterized. Ablation analysis used in conjunction with these properties provides a very satisfactory ability to determine ablator thickness requirements for a given flight trajectory and to predict internal ablator and backface temperature rise during thermal exposure.

Technological deficiencies for ablators in multi-pass heating environments are primarily associated with uncertainties arising from the fact that a number of environmental parameters were not investigated in the test program. These environmental factors include:

1. Cold Soak: Charred ablators may be subjected to cold soak conditions during orbital space flight between entry heating passes. Thermal contractions during cold soak could propagate fissures in the ablator char and lead to more extensive cracking and char erosion during subsequent entries.

2. Vibration: Acoustic noise or vibrations resulting from entry or from attitude control rocket firings may be detrimental to the ablator char. The magnitude of the acoustic and vibration environment associated with aerobraking entry is as yet undefined.

3. Shear: Aerodynamic shear forces can dislodge the ablator char. Shear at the corner of the elliptical dome must be considered in final ablator selection.

4. Pressure: Char recession is a function of heating rate and pressure. While tests were conducted at peak heating rate levels, pressures were only 50 percent of flight conditions. The effects of full flight pressure in conjunction with peak heating rates on char performance must be evaluated experimentally.

5. Atmospheric Variations, Trajectory Dispersions and Safety Factors: Tests simulated nominal conditions for aerobraking entry. However, the heating rates, pressures and shears used in design of flight hardware must be higher than nominal values to account for atmospheric variations and trajectory dispersions.

While there is no reason to believe that silicone ablators will not perform satisfactorily when the above environmental factors are taken into consideration; nevertheless, the materials must be qualified by tests for the full flight environment. These tests should include:

1. Multipass plasma arc testing with intermittent cold soak;

2. Plasma arc shear flow tests;

3. Vibration testing of charred ablators;

4. Tests at full design heating rates and pressure rather than for nominal conditions;

5. Tests at higher than design heating rate, pressure and shear values to establish safety margins and reliability.

IX. REFERENCES

1. E. L. Strauss: Ablative and Metallic Heat Shields for Aerobraking Entry - Task B-1 Report, Contract NAS8-27161, Report MCR-72-324, Martin Marietta Aerospace, Denver Division, Denver, Colorado, December, 1972.

2. E. L. Strauss: Ablative and Metallic Heat Shields for Aerobraking Entry - Task B-2 Report, Contract NAS8-27161, Report MCR-73-2, Martin Marietta Aerospace, Denver Division, Denver, Colorado, January, 1973

Table 1 - Plasma Arc Test Point Calibration

Test Point	Heating Rate (BTU/ft^2-sec)	Enthalpy (BTU/lb)	Pressure (atm) Pitot Probe	Pressure (atm) Test Cell	Power (BTU/sec) To Arc Generator	Power (BTU/sec) In Gas	Gas Flow (lb/sec) Oxygen	Gas Flow (lb/sec) Nitrogen
3 in.-Diameter Nozzle								
1	115	4701	.065	.0065	244.8	117.5	.00575	.001925
2	80	3897	.057	.0067	172.9	97.4	.00575	.001925
3	55	2512	.055	.0070	109.4	75.4	.00690	.00231
4	27.5	2434	.036	.0069	63.5	36.5	.00345	.001155
10 in.-Diameter Nozzle								
1	20	4813	.0082	.00036	356.4	96.3	.0154	.0046
2	15	3518	.0063	.00016	184.5	70.4	.0154	.0046
3	14	3265	.0063	.00013	175.2	65.3	.0154	.0046
4	8	2315	.0049	.00029	99.9	46.3	.0154	.0046
5	6	2315	.0047	.00033	80.5	46.3	.0154	.0046

Table 2 - Test Conditions for Two-Pass Entry Simulation

Specimen Number	Material	Heating Rate (BTU/ft^2-sec)	Enthalpy (BTU/lb)	Stagnation Pressure (atm)	Pulse Duration (sec)
Low Drag Simulation - First Pass					
1	ESA-5500	115/25.2	4701/2434	.065/.036	50/200
2	ESA-5500	115/26.1	4701/2434	.065/.036	50/200
5	ESA-3560	115/24.8	4701/2434	.065/.036	50/200
Low Drag Simulation - Second Pass					
1	ESA-3560	84/24.8	3897/2434	.057/.036	90/360
2	ESA-3560	80/27.5	3897/2434	.057/.036	90/360
5	ESA-3560	81/28.9	3897/2434	.057/.036	90/360
High Drag Simulation - First Pass					
3	ESA-3560	80/32	3880/2437	.060/.032	50/200
4	ESA-3560	80/31	3957/2331	.060/.032	50/200
6	SLA-561	80/31	3957/2331	.060/.032	50/200
High Drag Simulation - Second Pass					
3	ESA-3560	55/31	2422/2319	.053/.032	80/300
4	ESA-3560	55.1/35.6	2422/2319	.054/.032	80/300
6	SLA-561	55.8/23.1	2187/2532	.054/.032	80/300

Table 3 - Comparison of Flight Environment with Proposed Test Plan Conditions and Actual Test Conditions Attained

	Peak Heating Rate (BTU/ft^2-sec)			Peak Enthalpy (BTU/lb)			Peak Stagnation Pressure (atm)		
	Flight	Test Plan	Test	Flight	Test Plan	Test	Flight	Test Plan	Test
2 Pass-Low Drag	127	120	115	19,900	6,000	4,701	.139	.070	.065
2 Pass-High Drag	85	80	80	20,870	4,500	3,957	.139	.070	.060
30 Pass-High Drag	21.5	20	20.2	20,950	5,000	4,830	.013	.0075	.0070

Table 4 - Test Conditions for 30-Pass and 15-Pass Heating

Test Cycle	Heating Rate (BTU/ft^2-sec)		Enthalpy (BTU/lb)		Stagnation Pressure (atm)	
	Average	Range	Average	Range	Average	Range
30-Pass Test; Specimens 1 and 2 (ESA-3560) and 5 (SLA-561)						
1 to 4	20.2/5.4	19.8-21.0/3.0-7.6	4830/2070	4490-5100/1500-2680	.0070/.0047	.0057-.0074/.0044-.0052
5 to 14	8.0	7.9-8.1	2510	2020-3210	.0052	.0039-.0062
15 to 24	8.0	7.4-8.9	2530	2030-3040	.0054	.0044-.0062
25 to 27	8.0	7.6-8.5	2800	2290-3740	.0055	.0053-.0061
28 to 30	13.9/5.8	13.5-14.5/5.3-6.6	3530/2060	3220-4070/1760-2680	.0064/.0048	.0061-.0069/.0046-.0053
15-Pass Test; Specimens 3 and 4 (ESA-3560) and 6 (SLA-561)						
1 to 5	20.2/5.7	19.8-20.4/4.8-8.1	5200/2200	4850-5780/2030-2630	.0075/.0050	.0070-.0082/.0047-.0055
6 to 10	19.8/5.7	19.2-20.4/4.0-6.6	4930/2380	4310-5400/1880-3180	.0074/.0051	.0072-.0076/.0042-.0058
11 to 15	15.8/5.7	15.0-20.0/3.3-6.6	3370/1870	2840-3710/1650-2170	.0065/.0050	.0063-.0070/.0047-.0067

Table 5 - Char Formation in Multi-Pass Test Models

Ablator	Test Environment	Predicted Decomposition		Measured Char Thickness		Change in Ablator Thickness (in.)
		Char Thickness (in.)	Pyrolysis Zone Thickness (in.)	Average (in.)	Range (in.)	
ESA-5500	2 Pass-Low Drag	.341*/.595	.130*/.178	.434*/.702	.676-.718	+.017 to +.025
ESA-3560	2 Pass-Low Drag	-	-	1.106	.968-1.245	-.035
ESA-3560	2 Pass-High Drag	.386*/.633	.118*/.182	.450*/.745	.730-.759	+.013 to -.003
SLA-561	2 Pass-High Drag	-	-	.890	.880-.900	-.094
ESA-3560	30 Pass-High Drag	0.832	0.284	.797	.764-.828	+.013 to +.022
SLA-561	30 Pass-High Drag	-	-	1.148	1.132-1.165	-.046
ESA-3560	15 Pass-High Drag	0.483	0.177	.431	.424-.437	+.017 to +.040
SLA-561	15 Pass-High Drag	-	-	.625	.563-.688	-.031

*After First Entry Pass

Table 6 - Comparison of Analytically Predicted and Measured Temperature Rise at End of Heating Pulse for Two-Pass Heating

Thermocouple Location (Distance from Front Face - in.)	Low Drag; First Pass (250 sec)			Low Drag; Second Pass (450 sec)		
	Analysis (°F) ESA-5500	Model 1 (°F) ESA-5500	Model 2 (°F) ESA-5500	Analysis (°F) ESA-5500	Model 1 (°F) ESA-5500	Model 2 (°F) ESA-5500
Surface	1800	1950	-	1905	-	2015
0.11	1500	1700	1800	1800	1900	-
0.33	1035	1240	950	1500	1575	1415
0.59	310	225	200	985	985	1015
1.21	15	15	10	125	90	105
Backface-2.03	0	15	-	0	-	105
	High Drag; First Pass (250 sec)			High Drag; Second Pass (380 sec)		
	Analysis (°F) ESA-3560	Model 3 (°F) ESA-3560	Model 4 (°F) ESA-3560	Analysis (°F) ESA-3560	Model 3 (°F) ESA-3560	Model 4 (°F) ESA-3560
Surface	2190	1900	1890	2025	2025	1975
0.105	1890	1700	1650	1935	-	1825
0.31	1260	1265	1275	1560	1690	1700
0.49	725	575	610	1150	1400	1300
0.815	60	90	210	540	550	390
Backface-1.36	0	25	75	10	125	100

Table 7 - Comparison of Analytically Predicted and Measured Temperature Rise at End of Heating Pulse for 30-Pass Heating

Thermocouple Location (Distance from Front Face - in.)	PASS 1			PASS 5			PASS 15		
	Analysis (^oF)	Model 1 (^oF)	Model 2 (^oF)	Analysis (^oF)	Model 1 (^oF)	Model 2 (^oF)	Analysis (^oF)	Model 1 (^oF)	Model 2 (^oF)
Surface	1121	-	-	1346	1620	1540	1371	1515	1635
0.16-nominal	925	875	890	1211	-	1220	1279	1087	1360
0.36-nominal	448	440	450	945	690	688	1071	756	1080
0.66-nominal	30	85	75	440	62	69	763	267	357
1.37-nominal	0	0	0	3	0	0	26	0	12
Backface-2.25	0	0	0	0	0	0	0	0	0
	PASS 25			PASS 28			PASS 30		
	Analysis (^oF)	Model 1 (^oF)	Model 2 (^oF)	Analysis (^oF)	Model 1 (^oF)	Model 2 (^oF)	Analysis (^oF)	Model 1 (^oF)	Model 2 (^oF)
Surface	1385	-	-	1208	1540	1590	1211	-	-
0.16-nominal	1313	1302	1350	1159	1400	1400	1162	1435	1470
0.36-nominal	1158	-	-	1067	-	1270	1074	1210	-
0.66-nominal	899	593	650	886	797	870	895	940	-
1.37-nominal	176	65	68	265	120	123	313	142	142
Backface-2.25	1	-	10	2	14	19	3	28	28

Table 8 - Comparison of Analytically Predicted and Measured Temperature Rise at End of Heating Pulse for 15-Pass Heating

Thermocouple Location (Distance from Front Face - in.)	PASS 1			PASS 4			PASS 6		
	Analysis (°F)	Model 3 (°F)	Model 4 (°F)	Analysis (°F)	Model 3 (°F)	Model 4 (°F)	Analysis (°F)	Model 3 (°F)	Model 4 (°F)
Surface	1121	1520	1490	1155	1480	1640	1183	-	-
0.13-nominal	964	1020	1070	1068	1070	1220	1105	1190	1210
0.29-nominal	614	710	540	900	890	840	946	1020	880
0.65-nominal	76	40	57	289	64	66	413	90	71
1.32-nominal	0	0	0	2	10	0	5	10	0
Backface-2.25	0	0	0	0	0	0	0	0	0
	PASS 8			PASS 12			PASS 15		
	Analysis (°F)	Model 3 (°F)	Model 4 (°F)	Analysis (°F)	Model 3 (°F)	Model 4 (°F)	Analysis (°F)	Model 3 (°F)	Model 4 (°F)
Surface	1192	-	-	1183	1460	1540	1186	1400	1620
0.13-nominal	1119	1260	1340	1118	1270	1230	1122	1050	1150
0.29-nominal	966	1060	990	976	1110	970	988	950	850
0.65-nominal	483	102	110	559	104	123	611	95	85
1.32-nominal	5	5	0	6	10	0	6	10	8
Backface-2.25	0	0	0	0	0	0	0	0	0

Table 9 - Comparison of Analytically Predicted and Measured Peak Backface Temperatures for Multi-Pass Heating

Model and Material	Initial Temperature for Final Pass (°F)	Peak Backface Temperature for Final Pass (°F)	Temperature Difference (°F)	Time of Peak Temperature (from start of final pass - sec)
<u>**2-Pass; Low Drag**</u>				
Analysis; ESA-5500	115	177*	62	1160**
Model 1; ESA-5500	-	-	-	-
Model 2; ESA-5500	93	250	157	1026
Model 5; ESA-3560	102	292	190	510
<u>**2-Pass; High Drag**</u>				
Analysis; ESA-3560	175	282	107	1072
Model 3; ESA-3560	80	349	269	795
Model 4; ESA-3560	93	364	271	845
Model 6; SLA-561	93	278	185	435
<u>**30-Pass; High Drag**</u>				
Analysis; ESA-3560	115	170*	55	1650**
Model 1; ESA-3560	140	171*	31	1200**
Model 2; ESA-3560	82	144*	62	1200**
Model 5; SLA-561	91	168	77	900
<u>**15-Pass; High Drag**</u>				
Analysis; ESA-3560	115	115*	0	280**
Model 3; ESA-3560	142	164	22	1440
Model 4; ESA-3560	98	123*	25	1050
Model 6; SLA-561	93	139*	46	1150

*Backface temperature still rising gradually

**Last data point

Table 10 - Ablative Heat Shield Weight

Entry Trajectory	Vehicle Configuration	Ablator Material	Total Ablator Weight (lb)	Comments
2 Pass	Low Drag	ESA-5500	1840	Not recommended - too heavy
2 Pass	Low Drag	ESA-3560	713*	Recommended Design
2 Pass	Low Drag	ESA-5500 to Arc Length = 71.4 in. then ESA-3560	1395	Conservative Design
2 Pass	High Drag	ESA-3560	678	Conservative Design
2 Pass	High Drag	SLA-561	379	Potential Minimum Weight Design
2 Pass	High Drag	ESA-3560 to Arc Length = 88.2 in. then SLA-561	622*	Recommended Design
30 Pass	Low Drag	ESA-3560	1056	Conservative Design
30 Pass	Low Drag	SLA-561	500	Potential Minimum Weight Design
30 Pass	Low Drag	ESA-3560 to Arc Length = 77.3 in. then SLA-561	859*	Recommended Design
30 Pass	High Drag	ESA-3560	972	Conservative Design
30 Pass	High Drag	SLA-561	437*	Recommended Design

*Weights of Recommended Designs

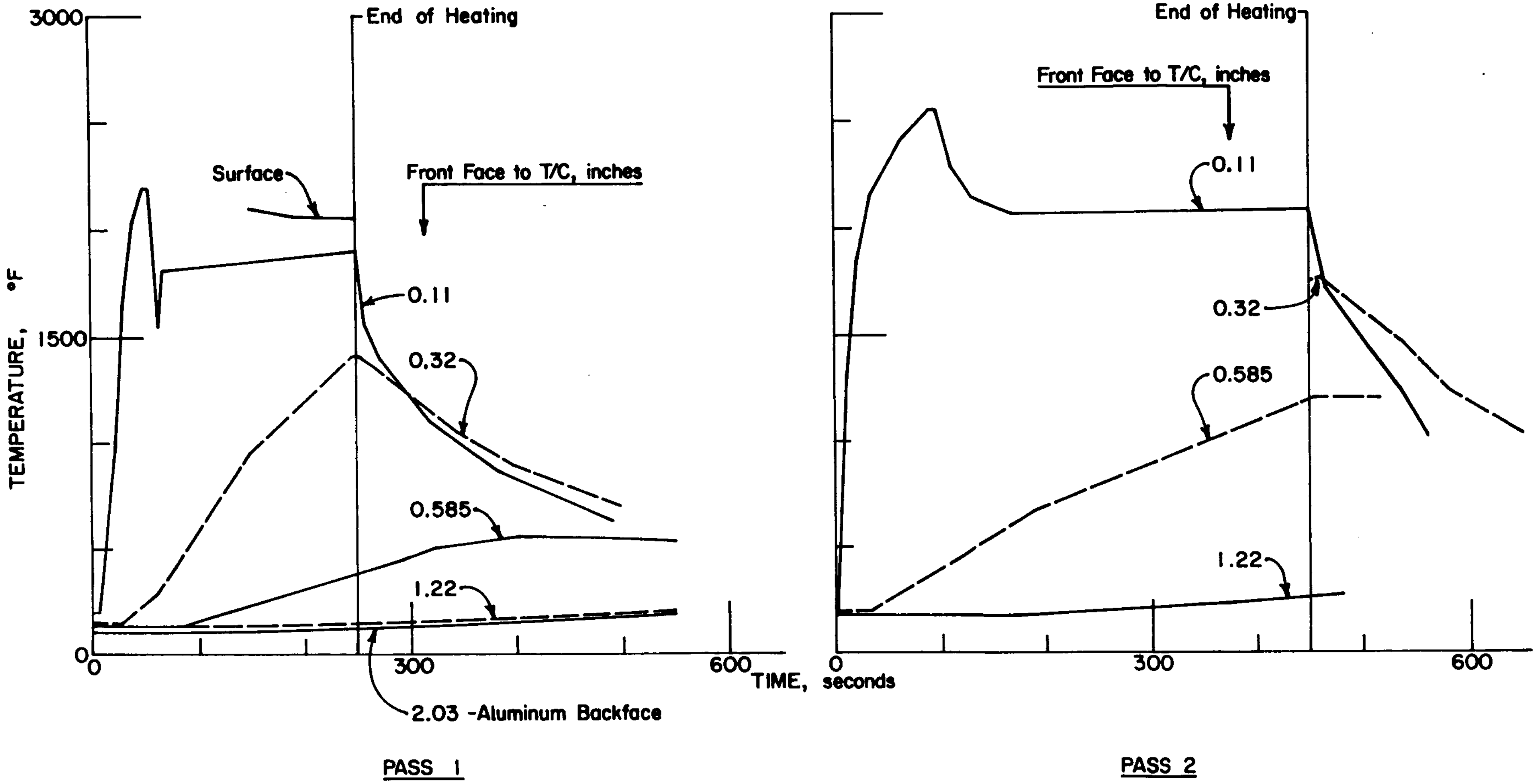

Figure 1 - Time-Temperature Traces for ESA-5500 Model No. 1 (Two-Pass Heating; Low Drag Configuration)

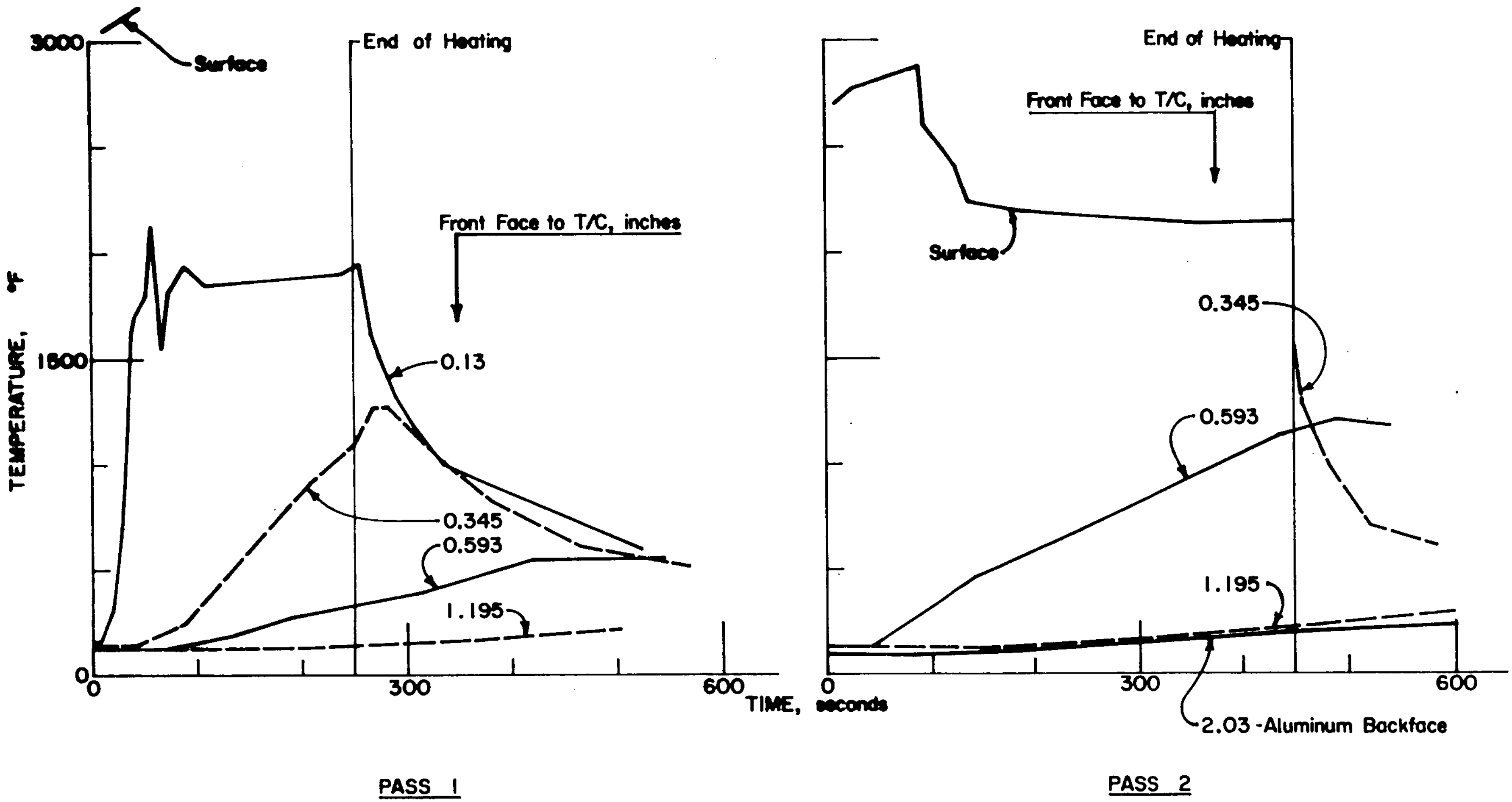

Figure 2 - Time-Temperature Traces for ESA-5500 Model No. 2 (Two-Pass Heating; Low Drag Configuration)

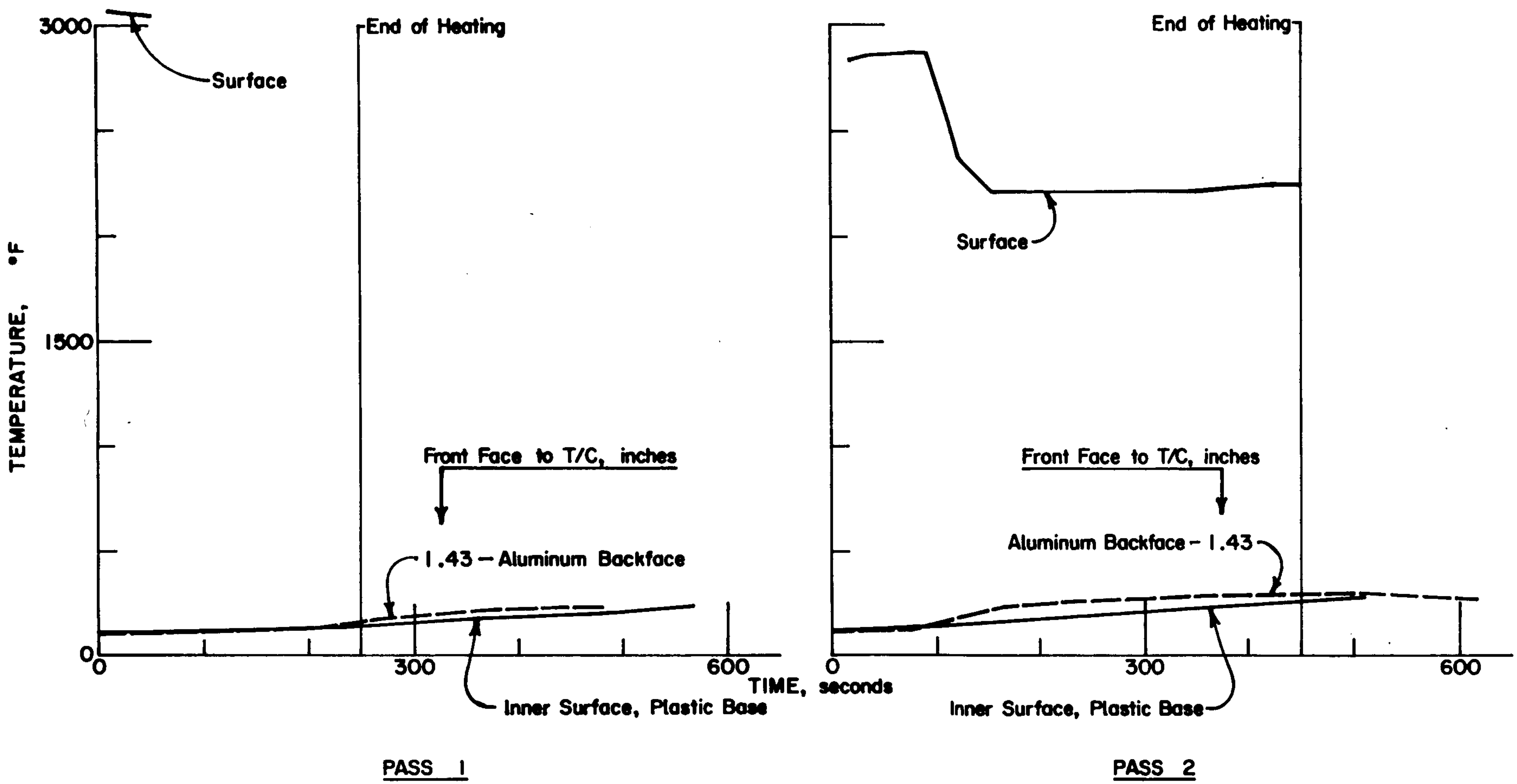

Figure 3 - Time-Temperature Traces for ESA-3560 Model No. 5 (Two-Pass Heating; Low Drag Configuration)

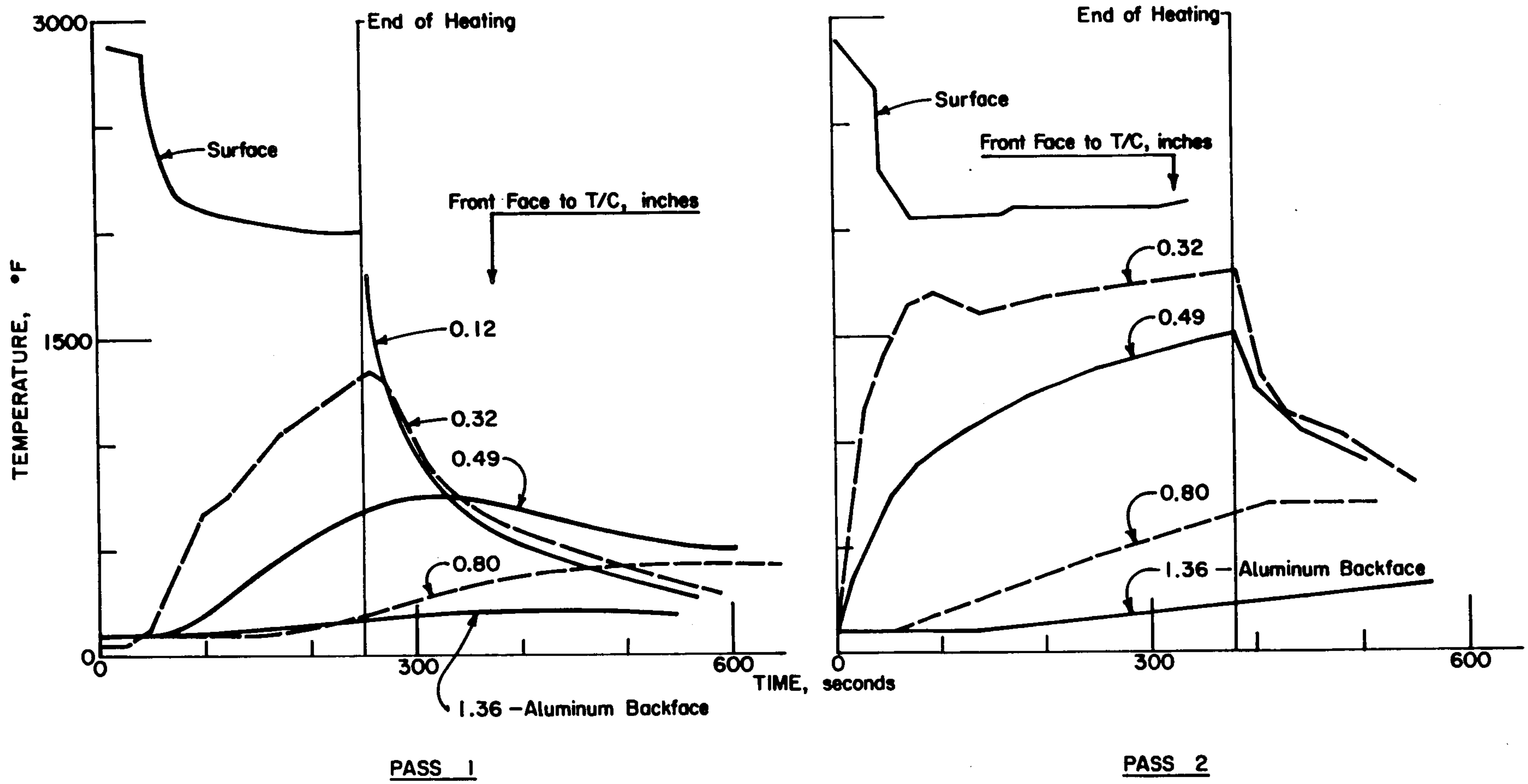

Figure 4 - Time-Temperature Traces for ESA-3560 Model No. 3 (Two-Pass Heating; High Drag Configuration)

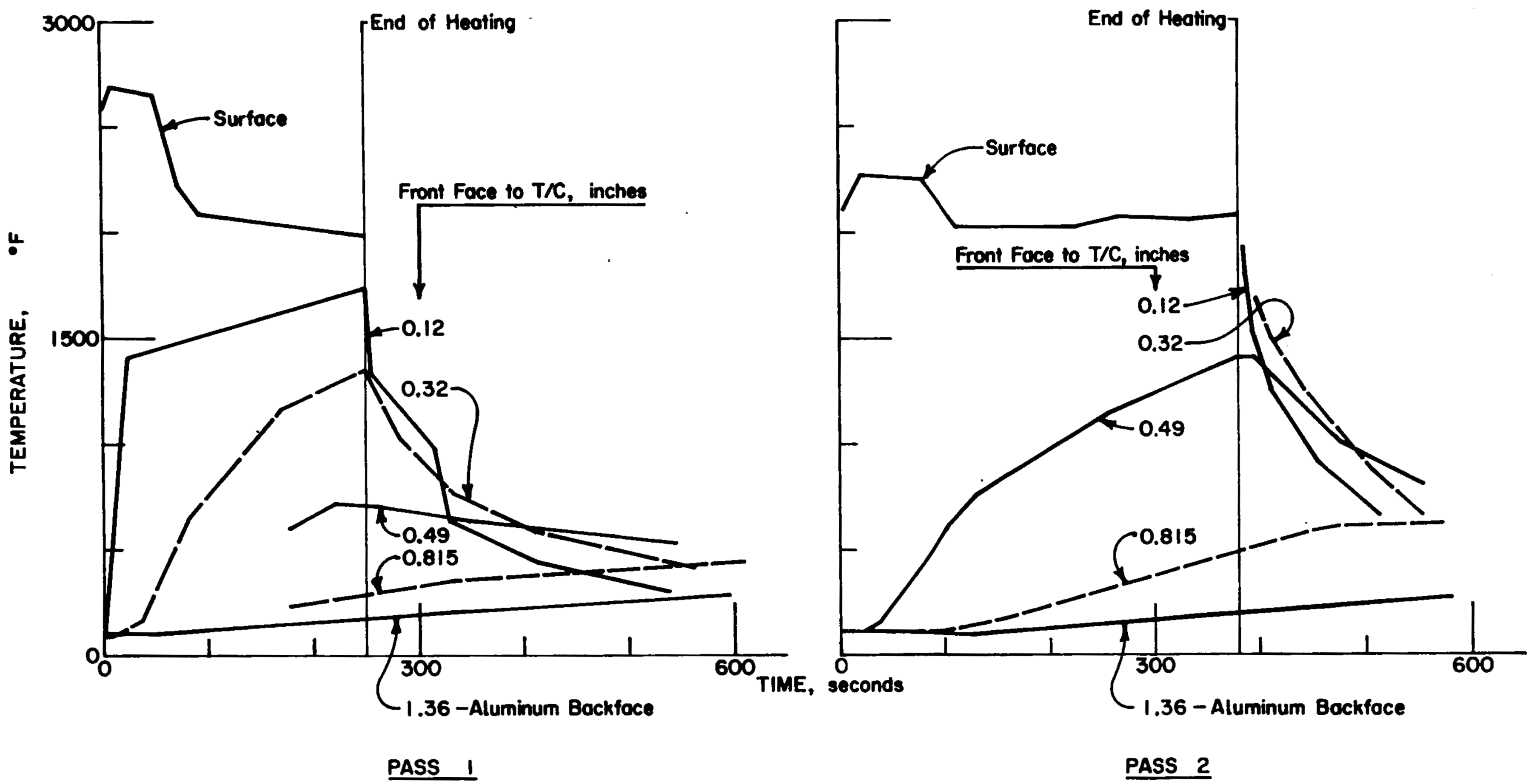

Figure 5 - Time-Temperature Traces for ESA-3560 Model No. 4 (Two-Pass Heating; High Drag Configuration)

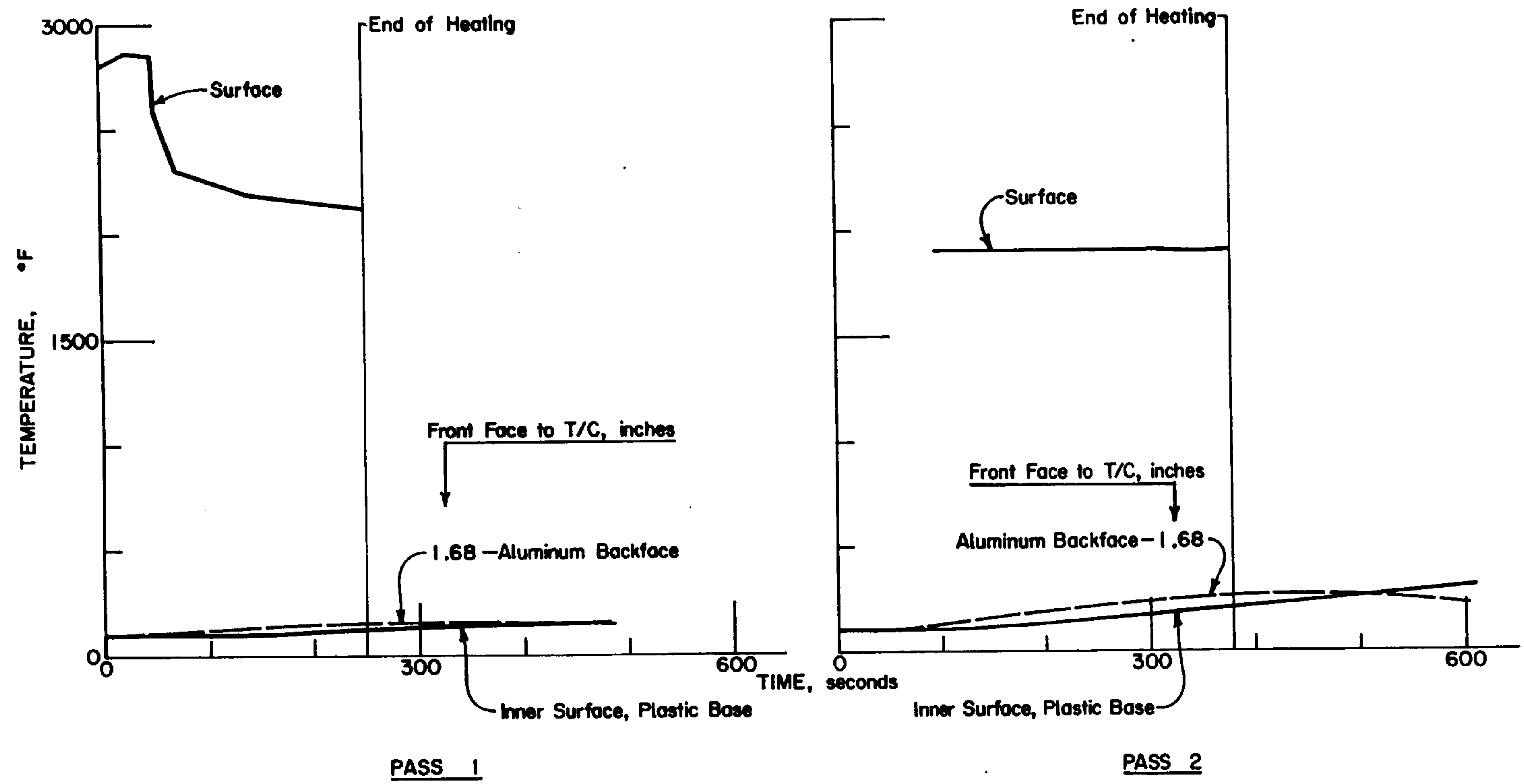

Figure 6 - Time-Temperature Traces for SLA-561 Model No. 6 (Two-Pass Heating; High Drag Configuration)

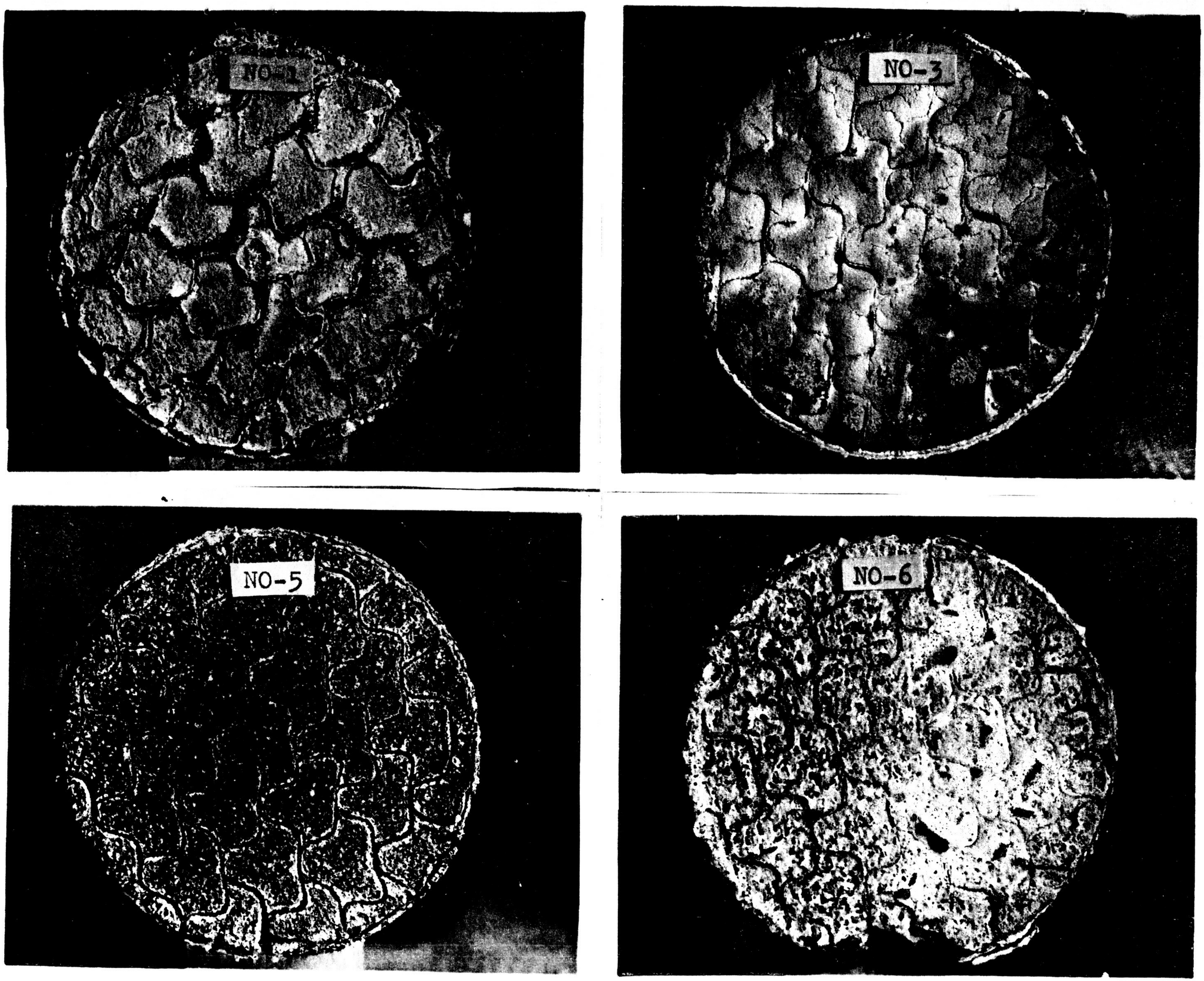

Figure 7 - Plasma Arc Models After 2-Pass Heating

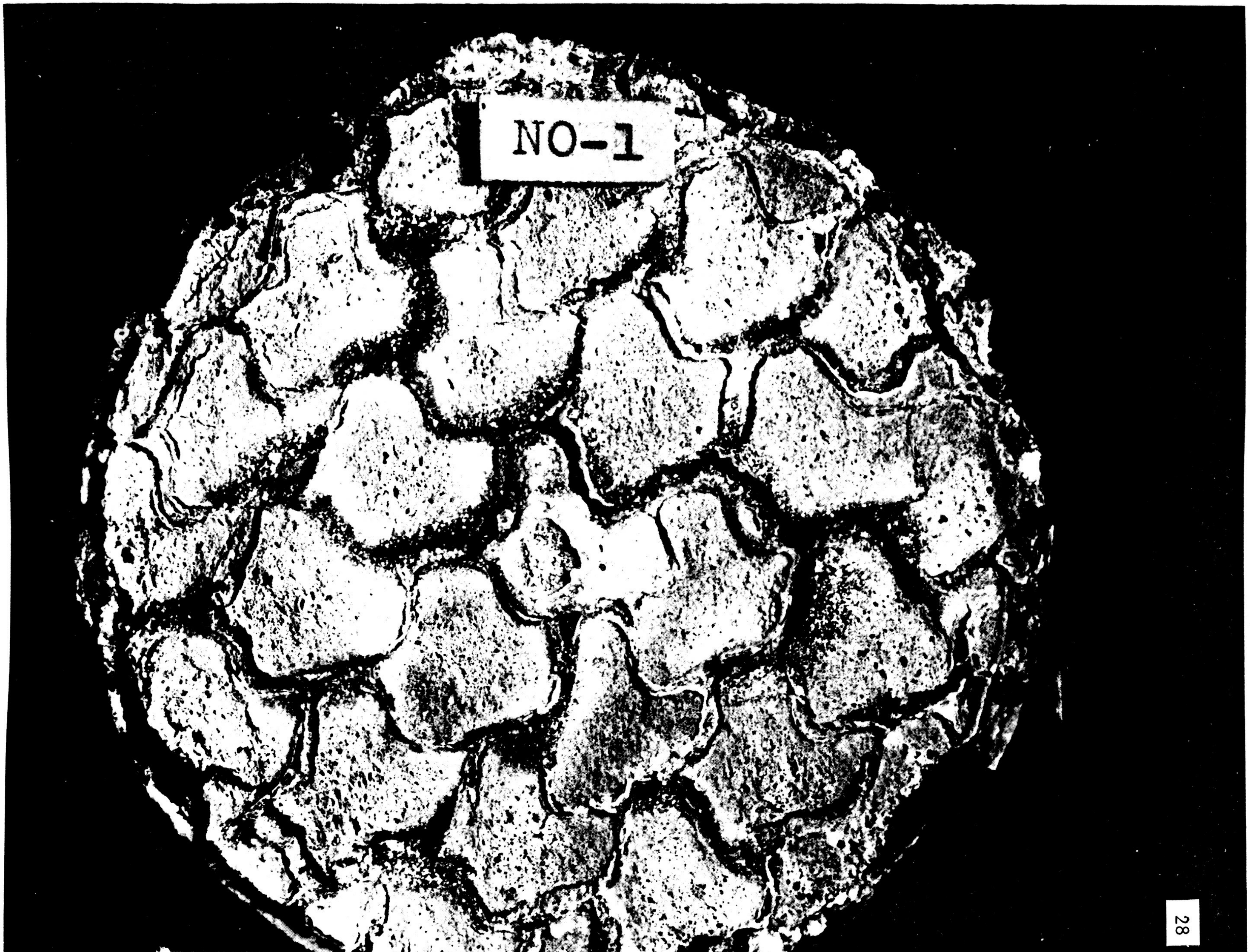

Figure 8 - 3X View of ESA-5500 Model No. 1 After 2-Pass, Low Drag Heating

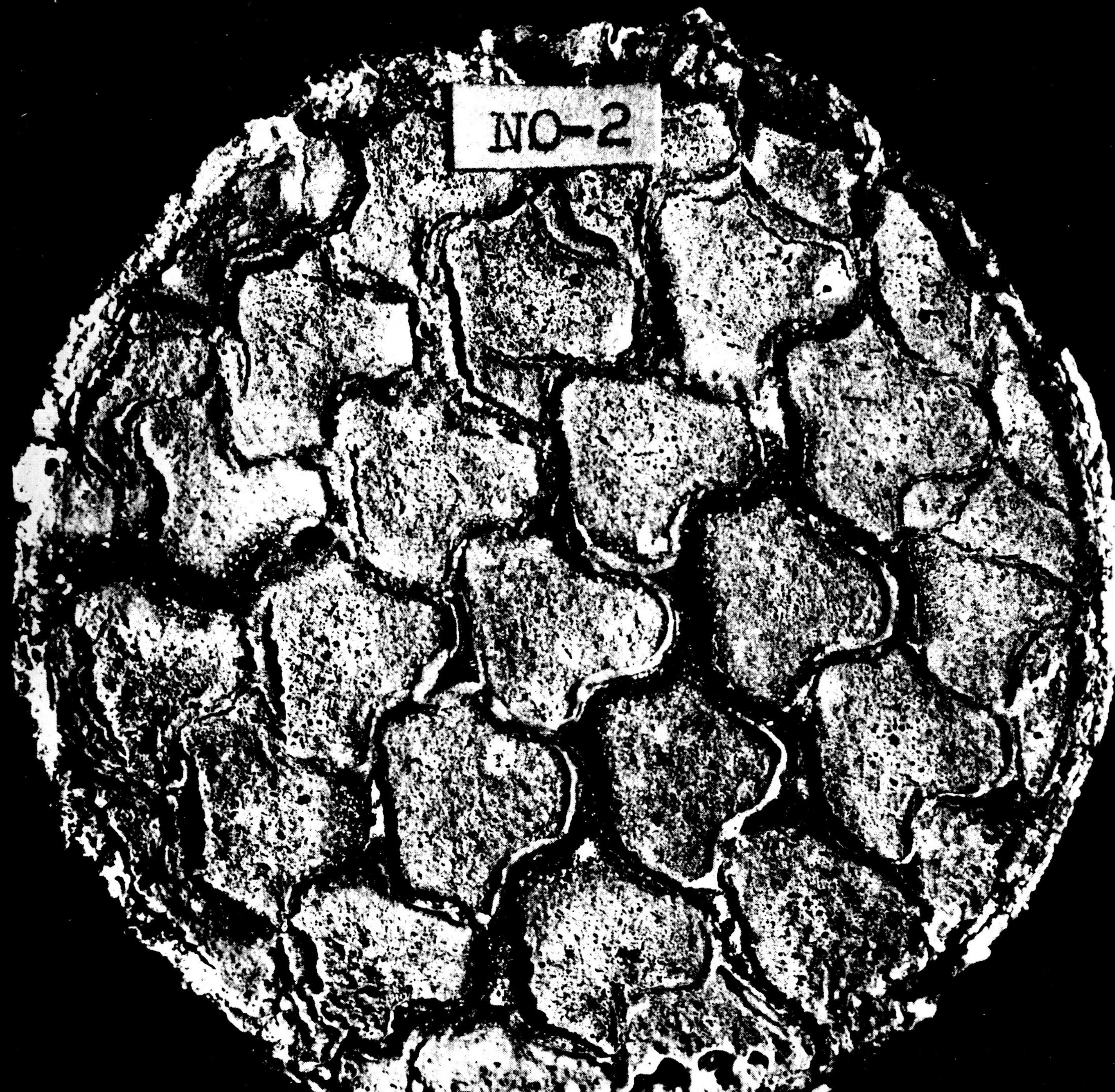

Figure 9 - 3X View of ESA-5500 Model No. 2 After 2-Pass, Low Drag Heating

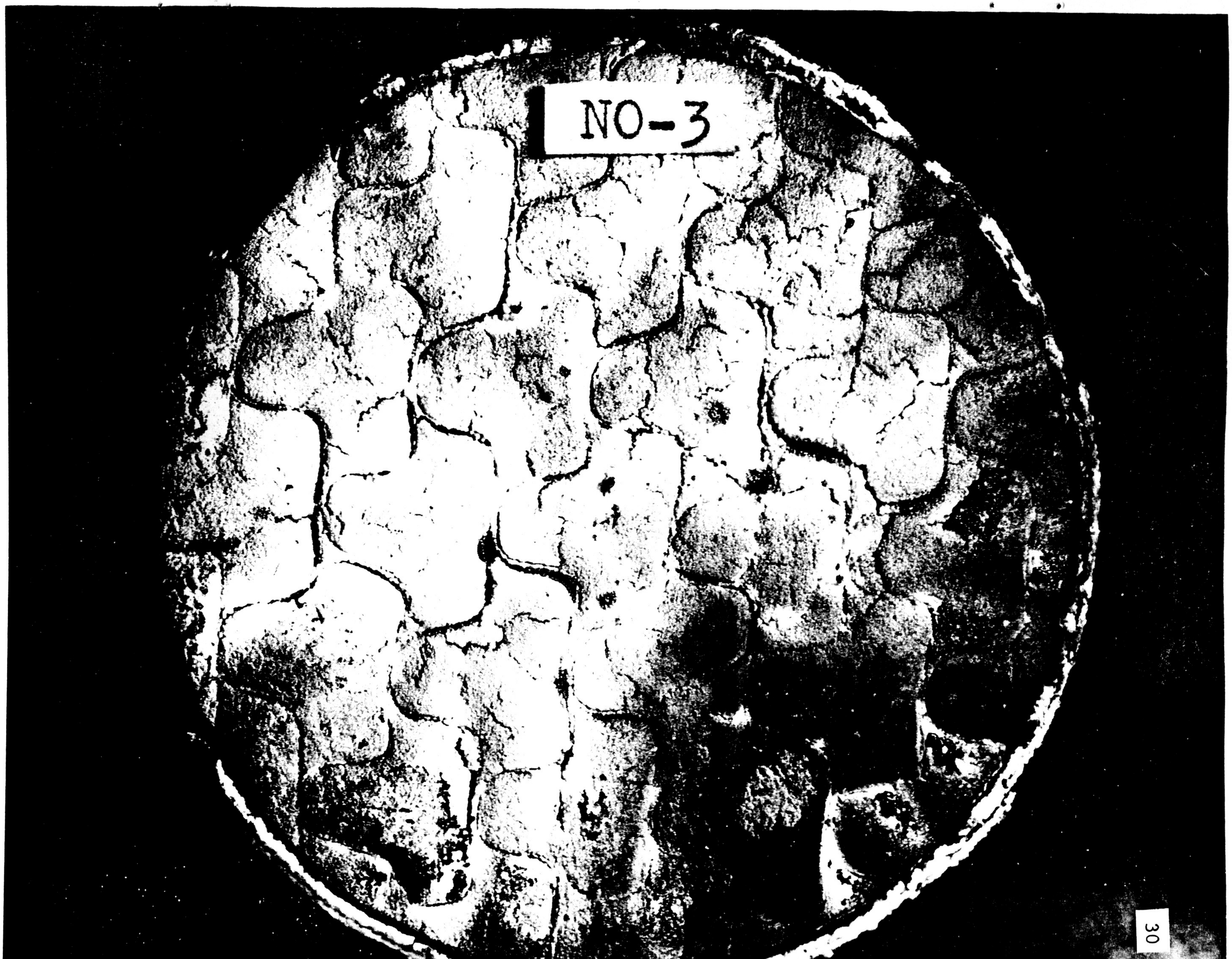

Figure 10 - 3X View of ESA-3560 Model No. 3 After 2-Pass, High Drag Heating

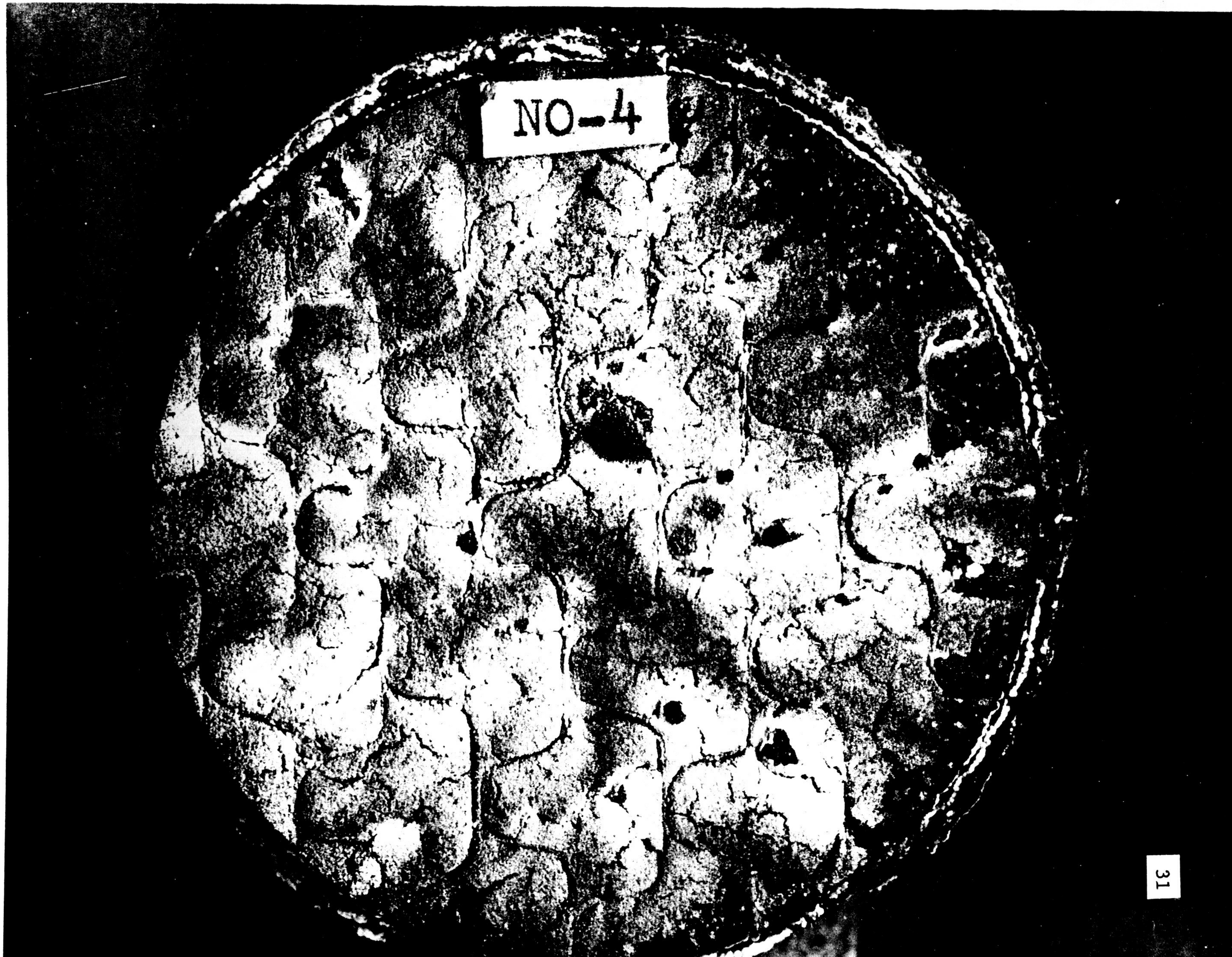

Figure 11 - 3X View of ESA-3560 Model No. 4 After 2-Pass, High Drag Heating

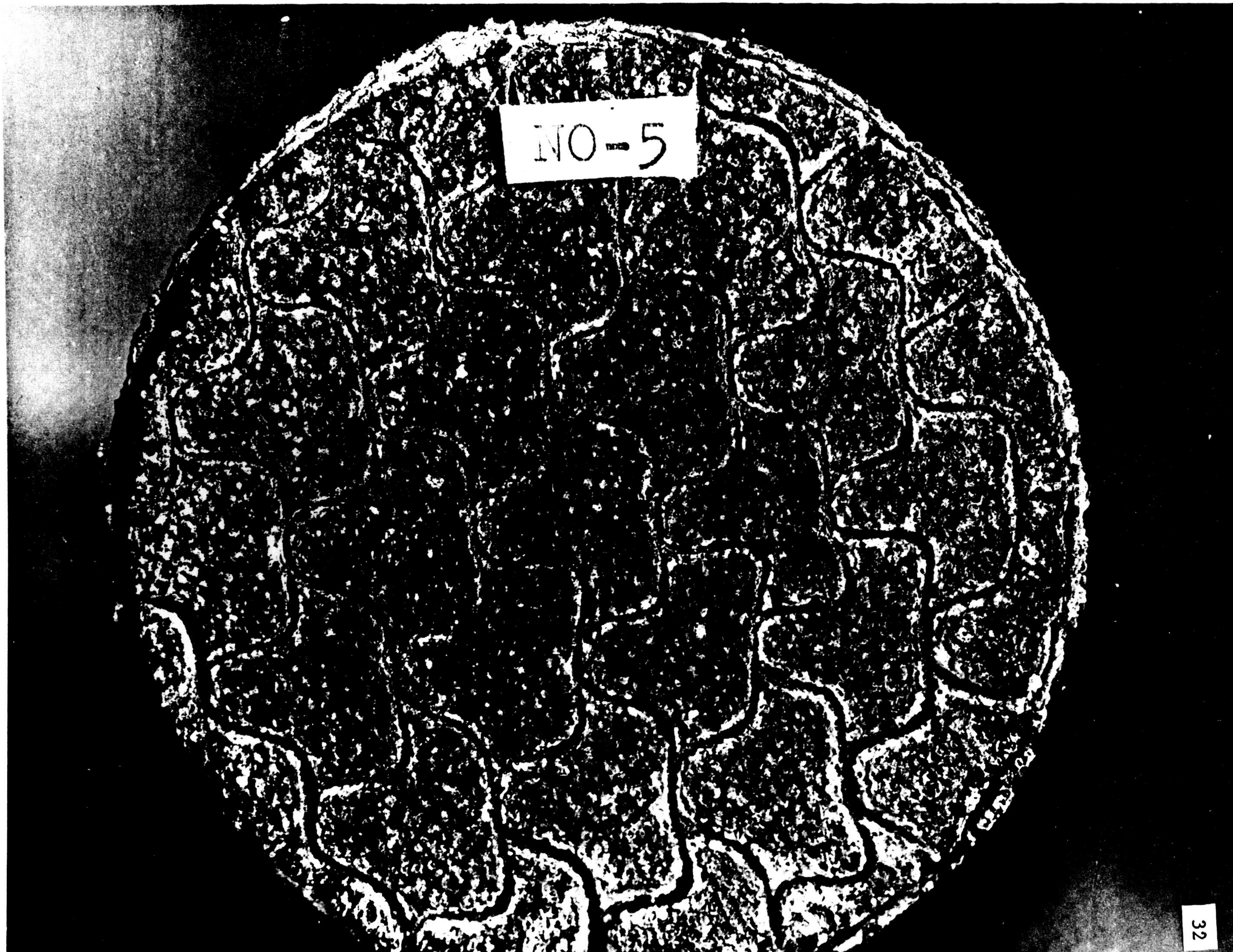

Figure 12 - 3X View of ESA-3560 Model No. 5 After 2-Pass, Low Drag Heating

Figure 13 - 3X View of SLA-561 Model No. 6 After 2-Pass, High Drag Heating

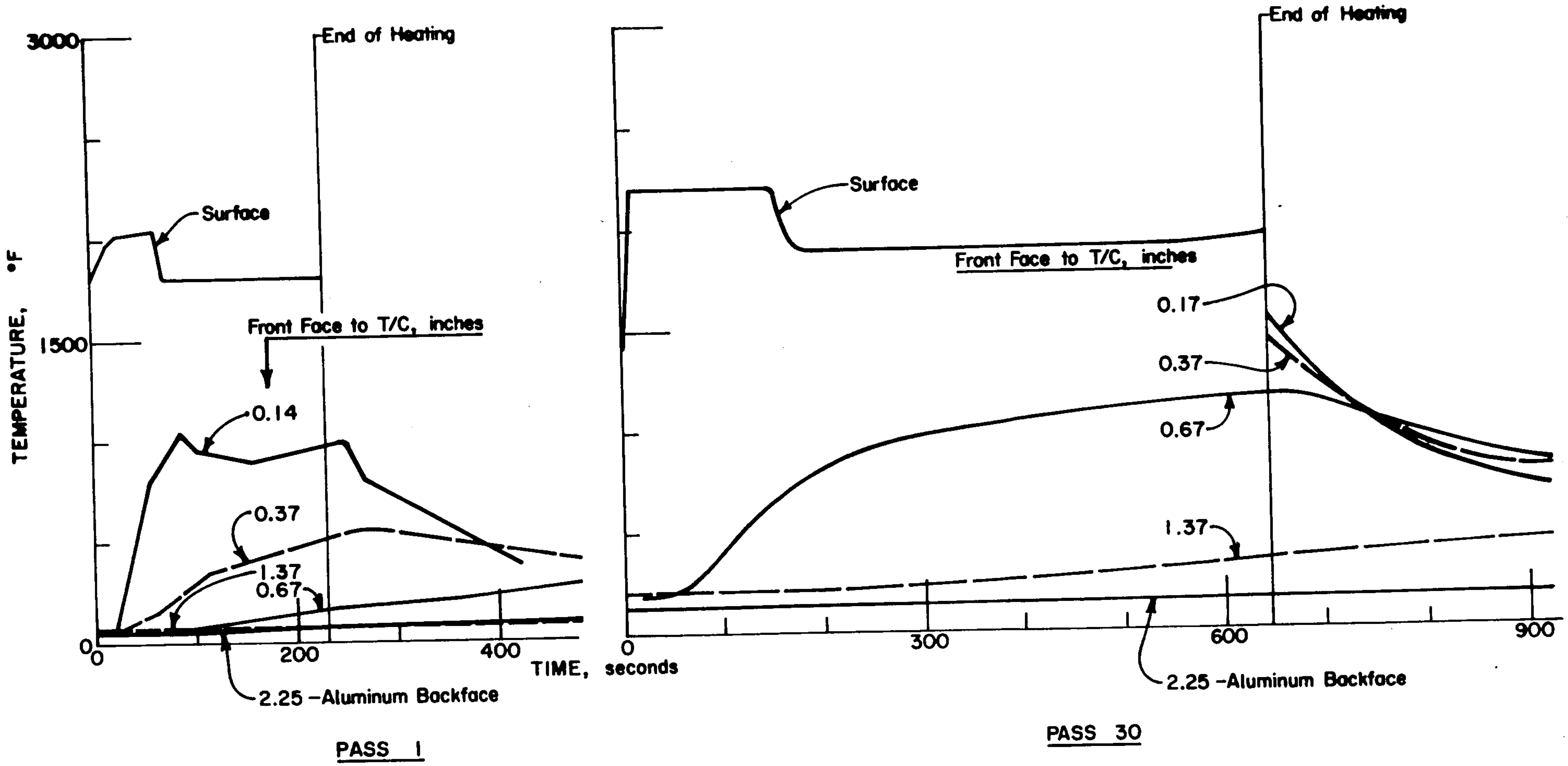

Figure 14 - Time-Temperature Traces for Passes 1 and 30, ESA-3560 Model No. 1 (30-Pass Heating)

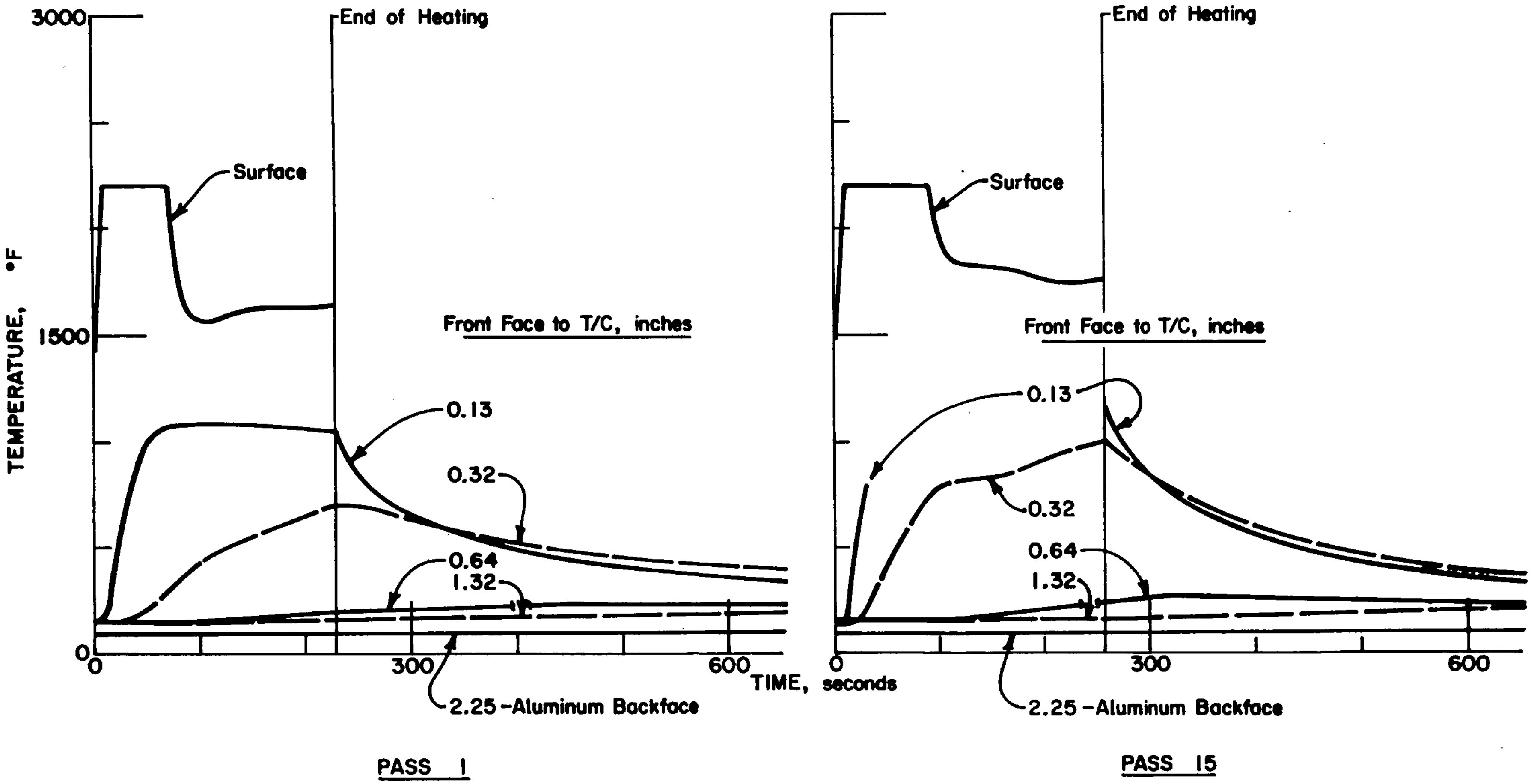

Figure 15 - Time-Temperature Traces for Passes 1 and 15, ESA-3560 Model No. 4 (15-Pass Heating)

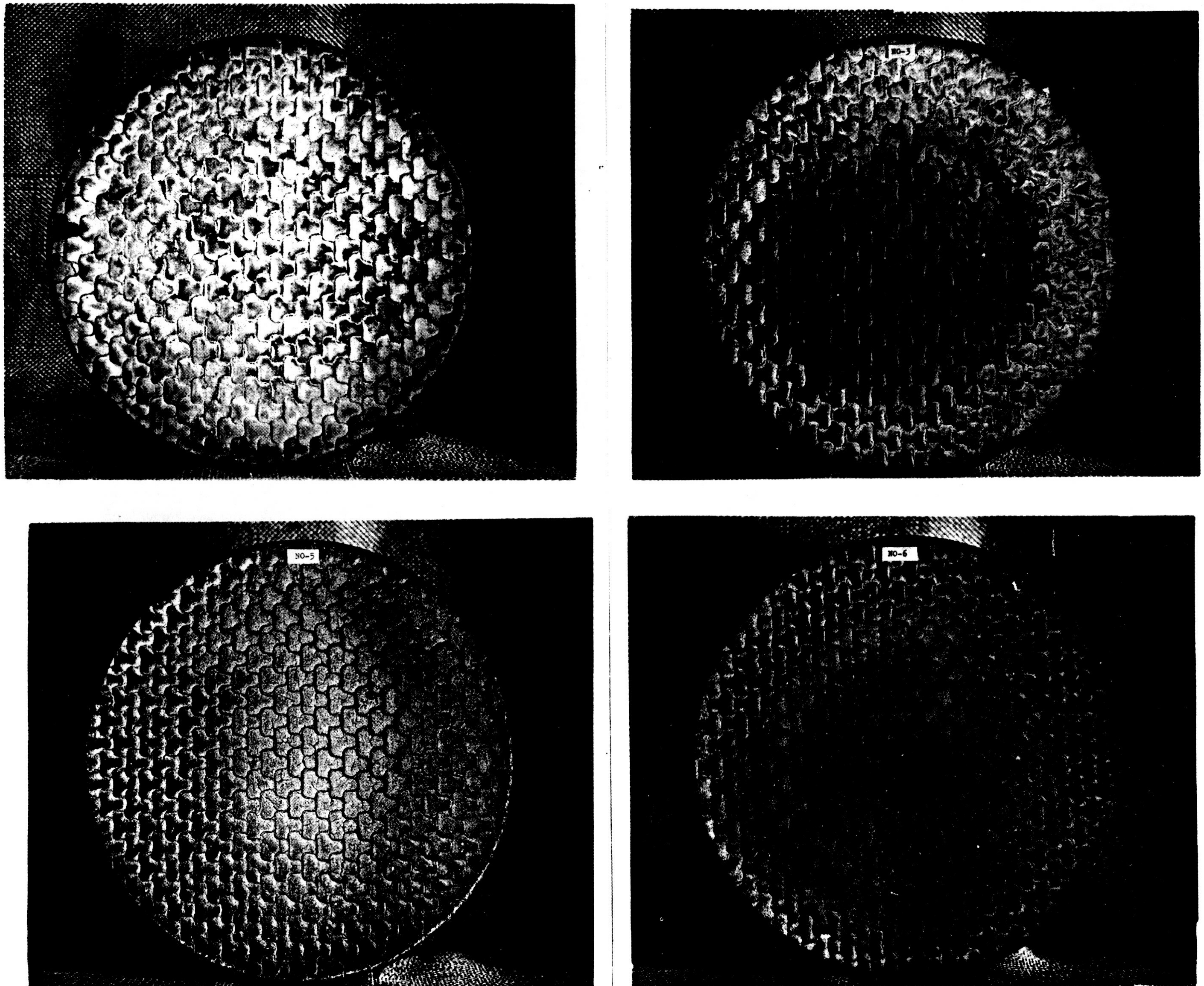

Figure 16 - Plasma Arc Models After 30-Pass and 15-Pass Heating

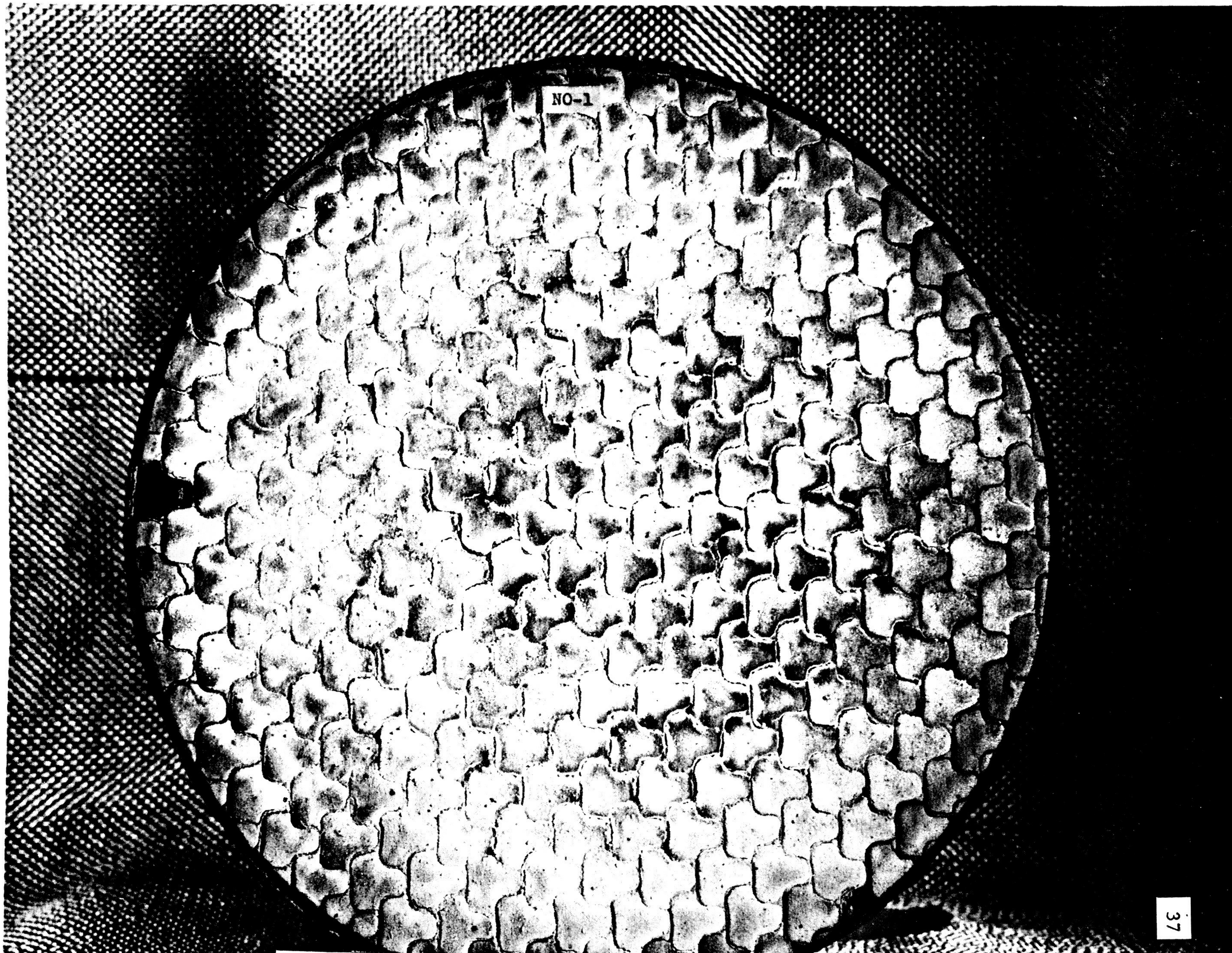

Figure 17 - ESA-3560 Model No. 1 After 30-Pass Heating

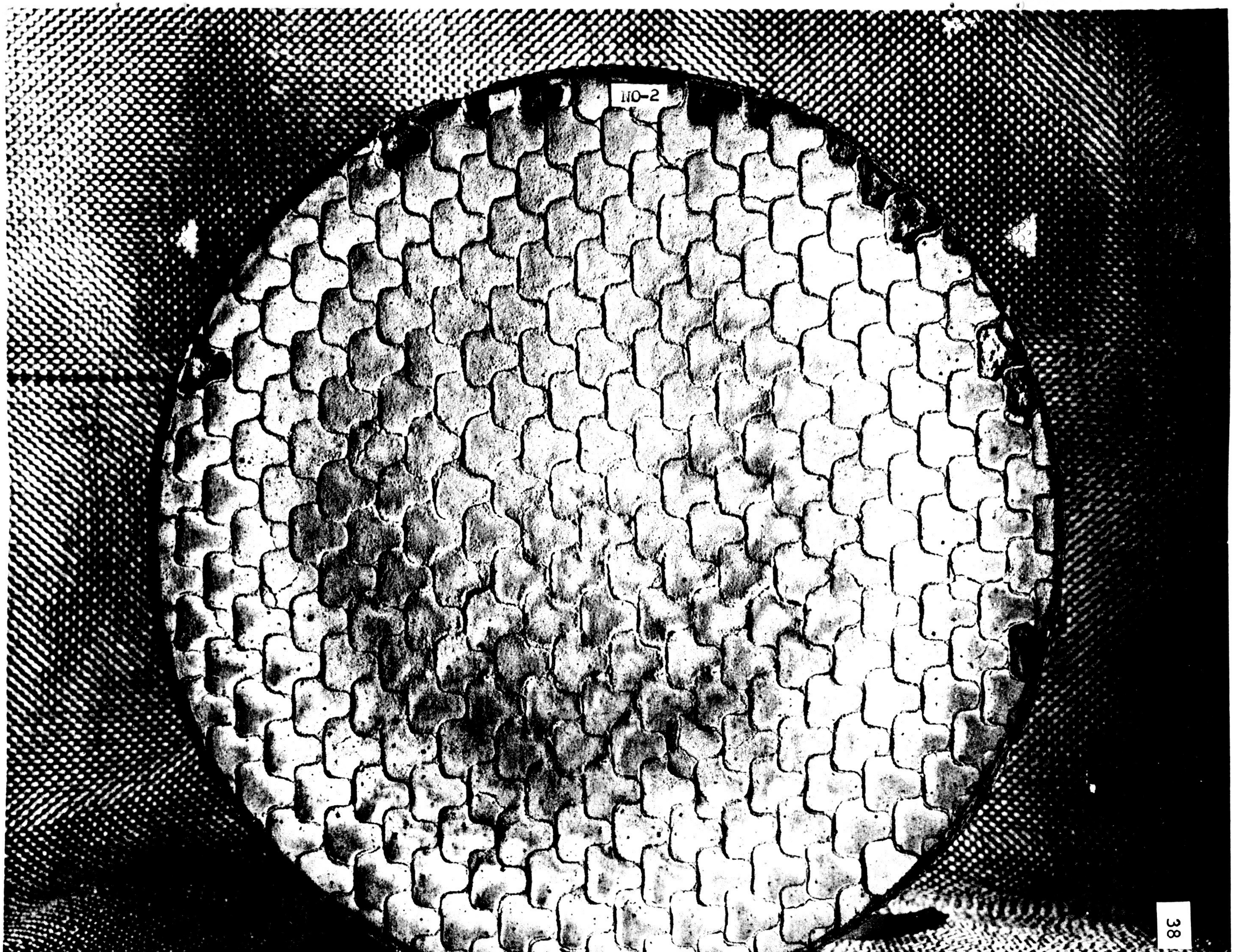

Figure 18 - ESA-3560 Model No. 2 After 30-Pass Heating

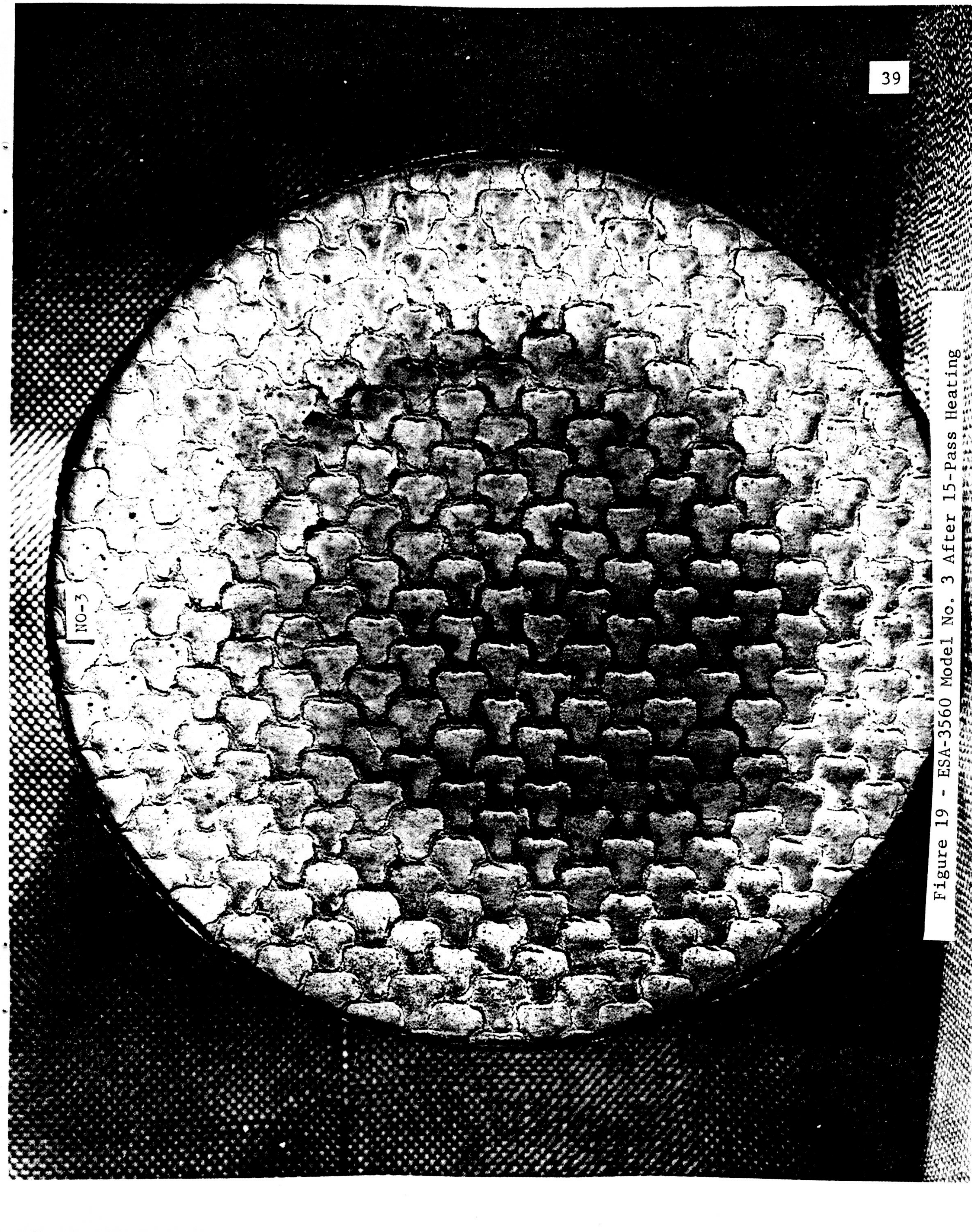

Figure 19 - ESA-3560 Model No. 3 After 15-Pass Heating

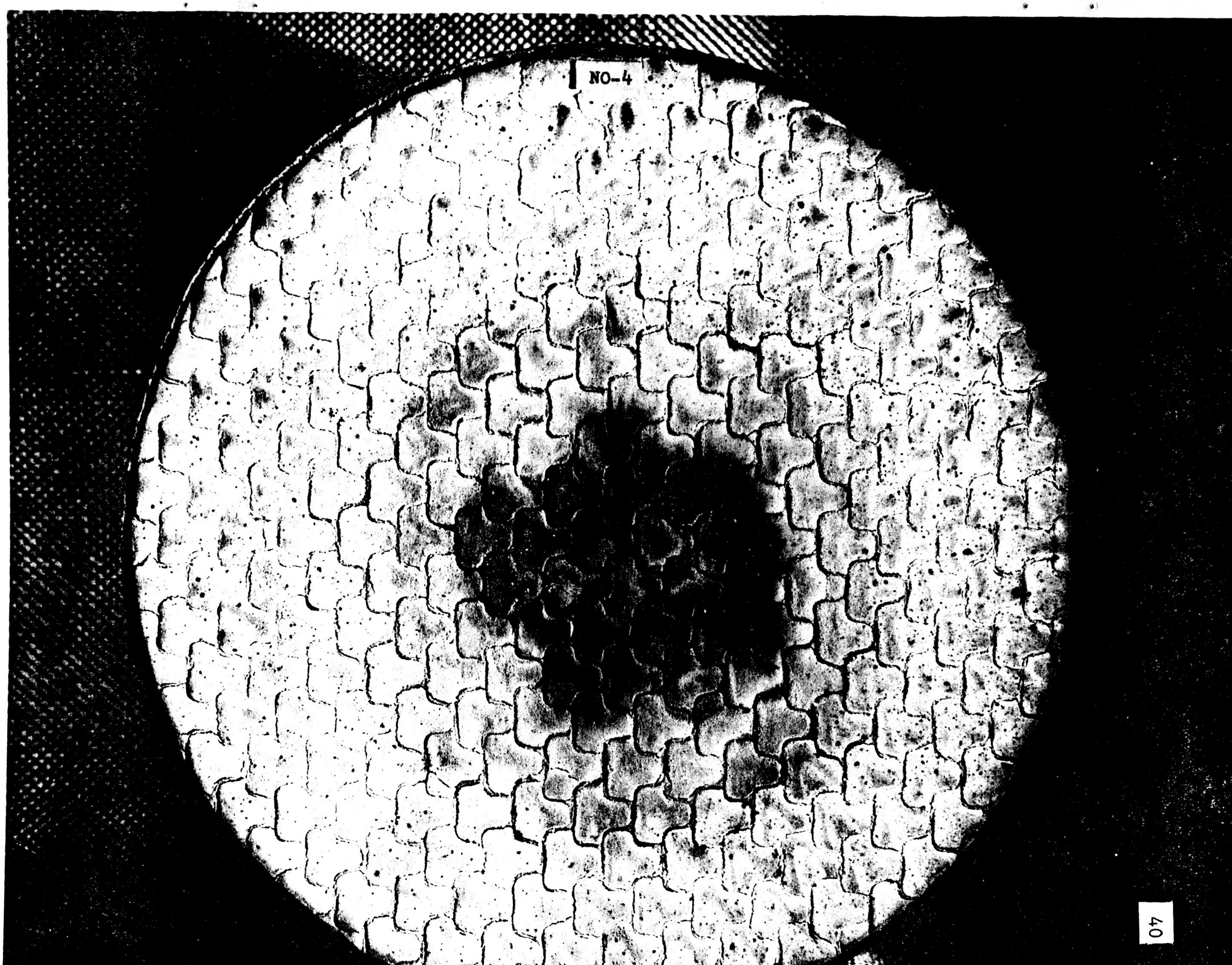

Figure 20 - ESA-3560 Model No. 4 After 15-Pass Heating

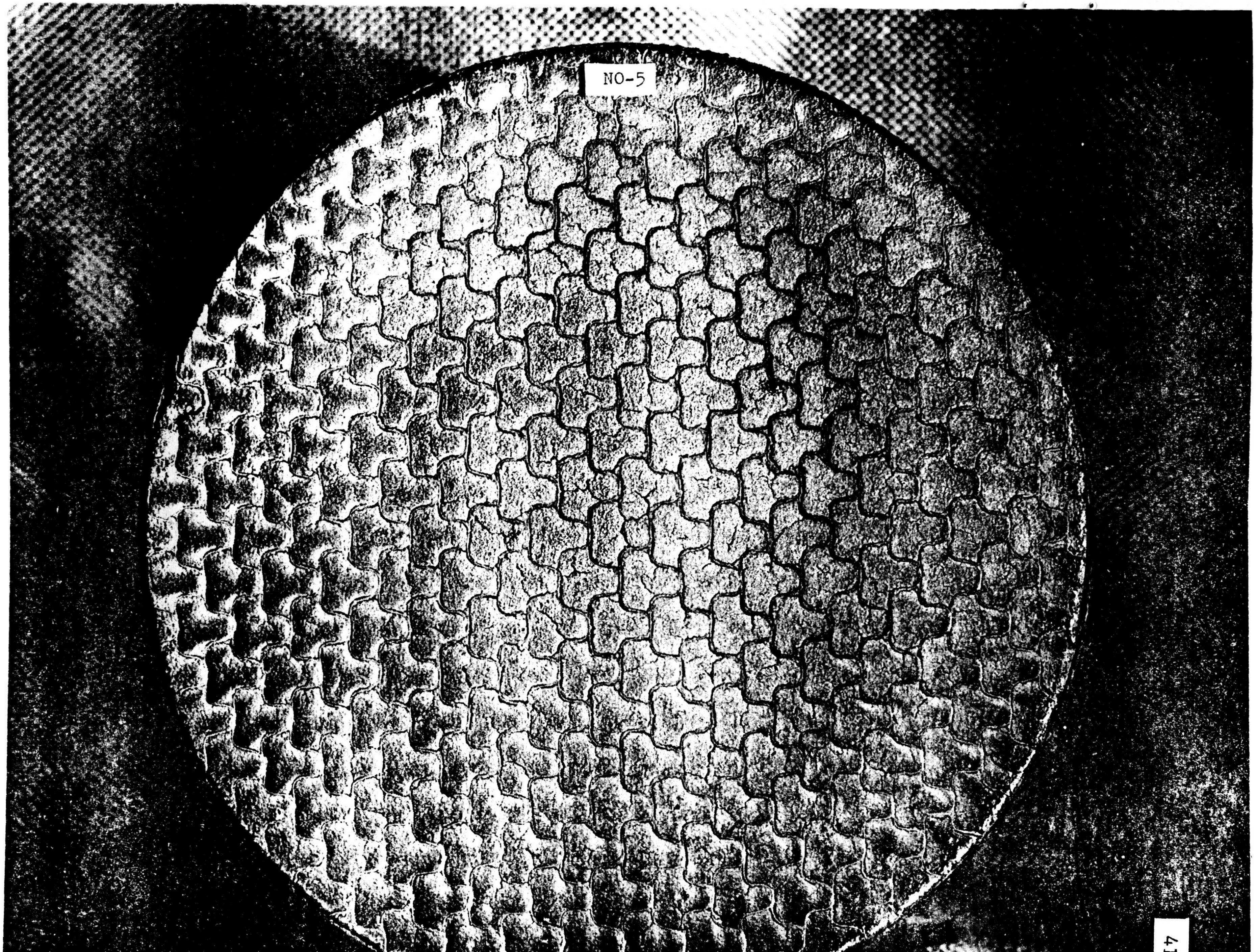

Figure 21 - SLA-561 Model No. 5 After 30-Pass Heating

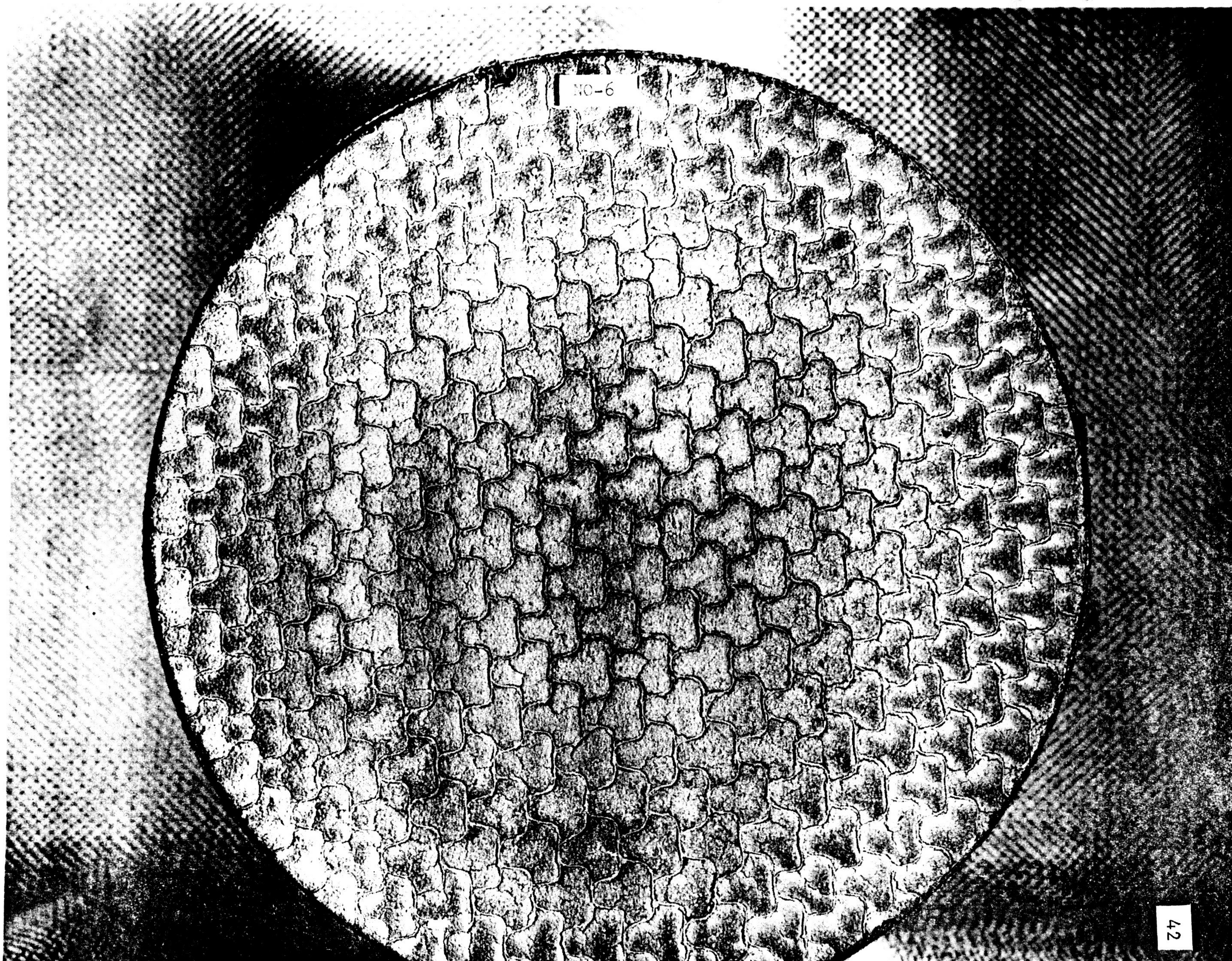

Figure 22 - SLA-561 Model No. 6 After 15-Pass Heating

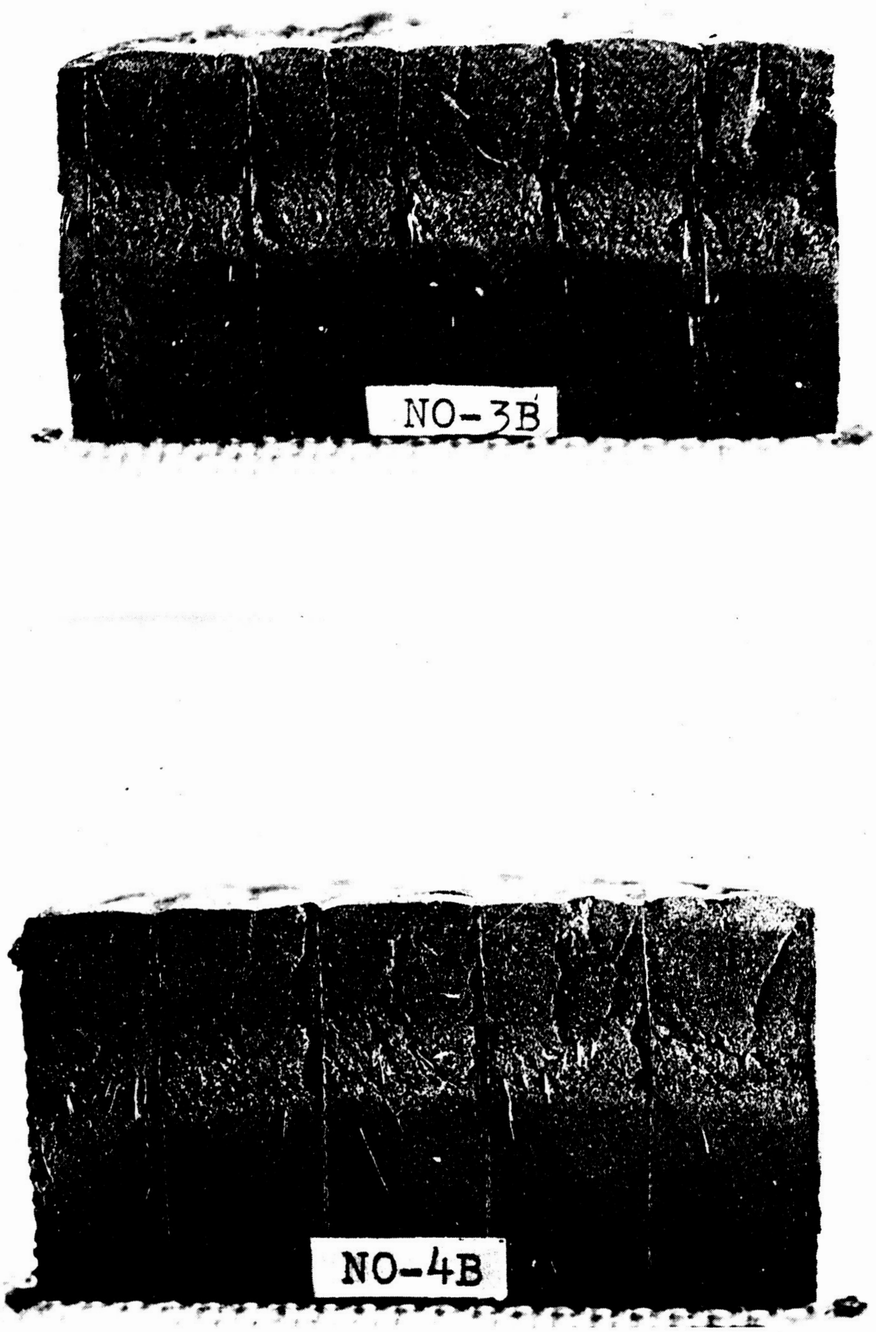

Figure 23 - Cross-Section of ESA-3560 Models After Exposure to Two-Pass, High Drag Heating

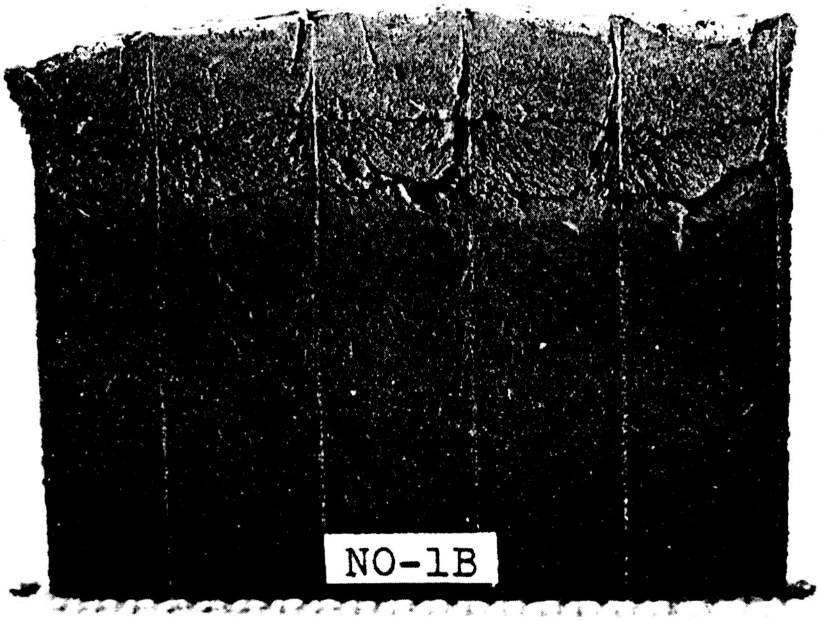

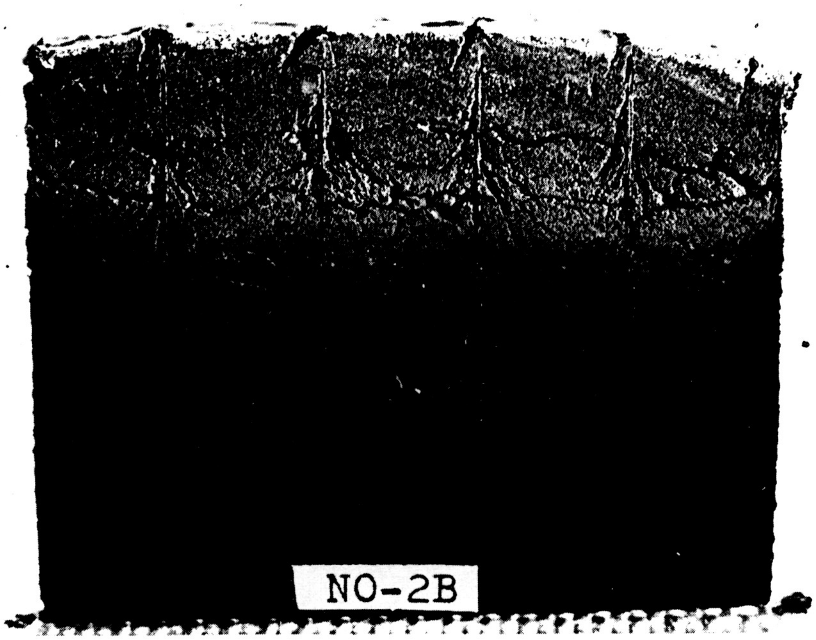

Figure 24 - Cross-Section of ESA-5500 Models After Exposure to Two-Pass, Low Drag Heating

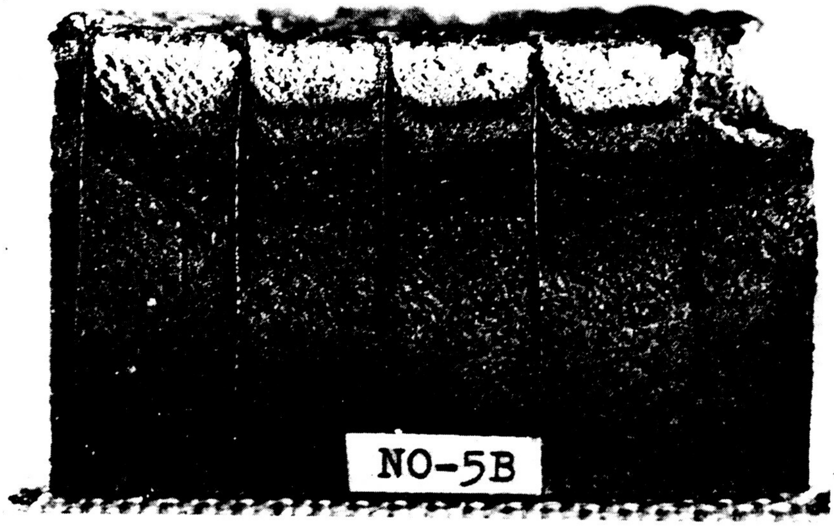

Figure 25 - Cross-Section of ESA-3560 Model After Exposure to Two-Pass, Low Drag Heating

Figure 26 - Cross-Section of SLA-561 Model After Exposure to Two-Pass, High Drag Heating

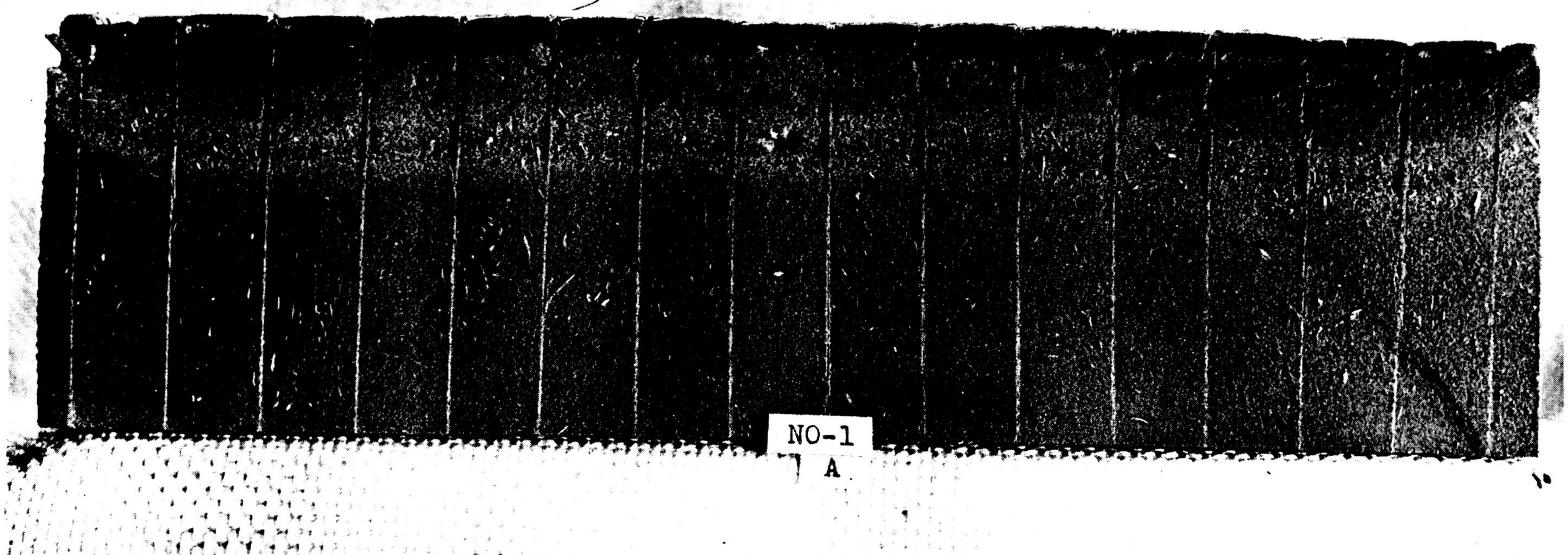

Figure 27 - Cross-Section of ESA-3560 Model No. 1 After 30-Pass Heating

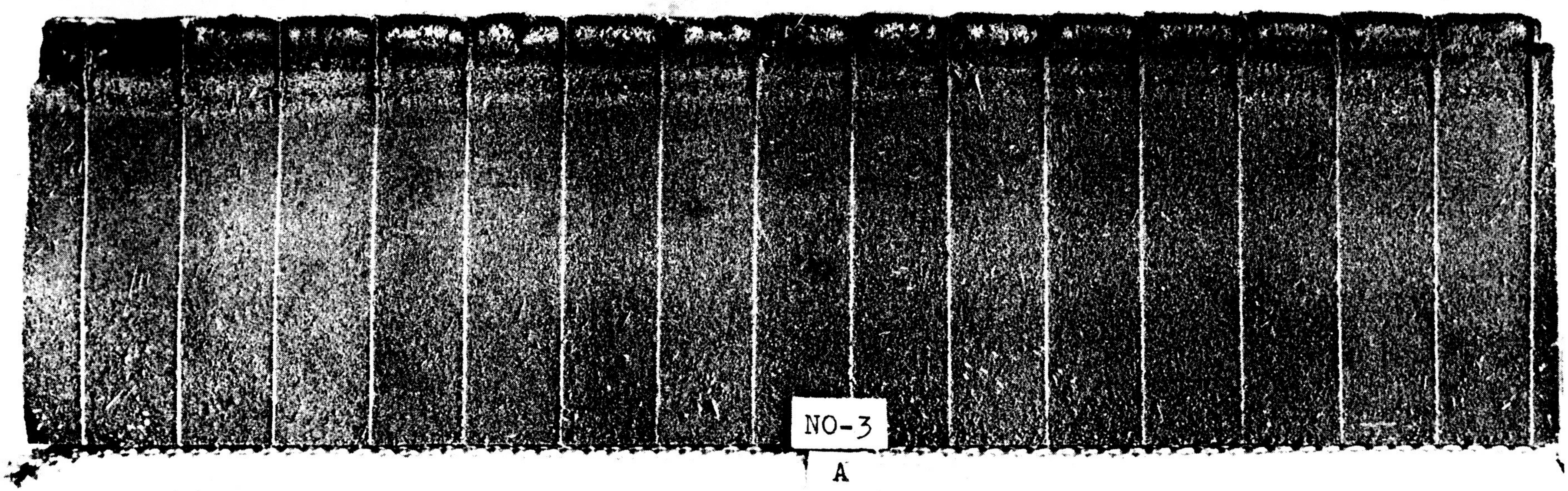

Figure 28 - Cross-Section of ESA-3560 Model No. 3 After 15-Pass Heating

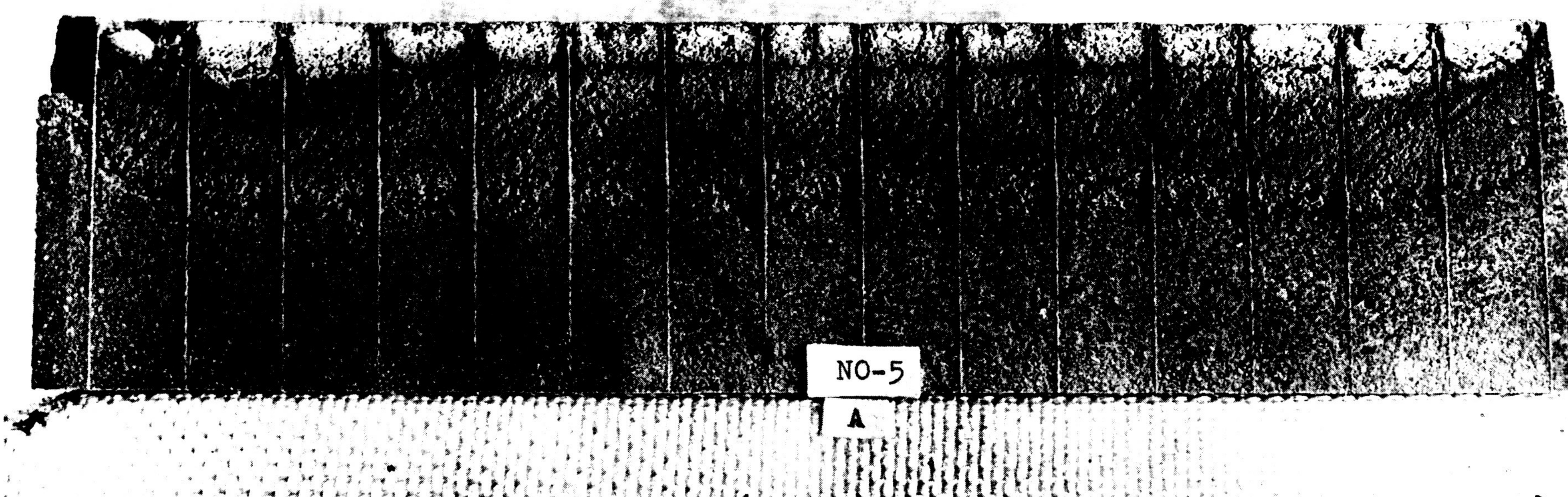

Figure 29 - Cross-Section of SLA-561 Model No. 5 After 30-Pass Heating

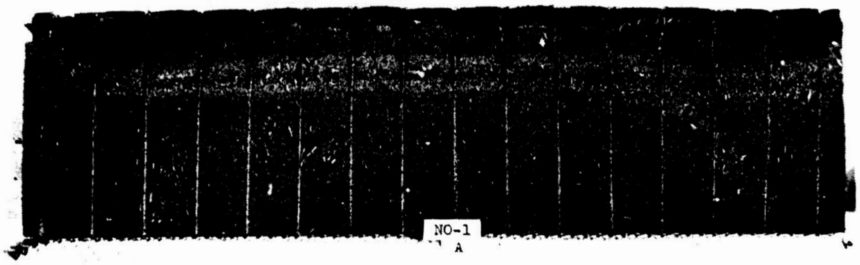

ESA-3560
30-Pass Heating

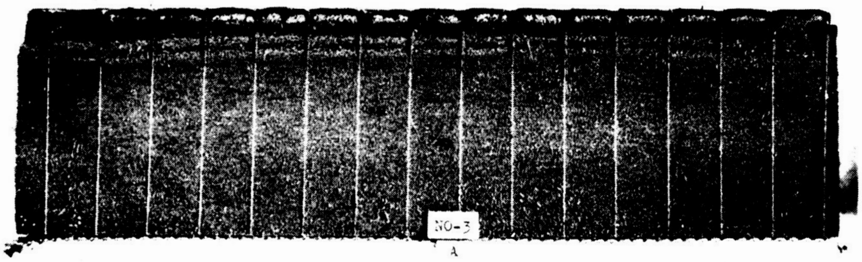

ESA-3560
15-Pass Heating

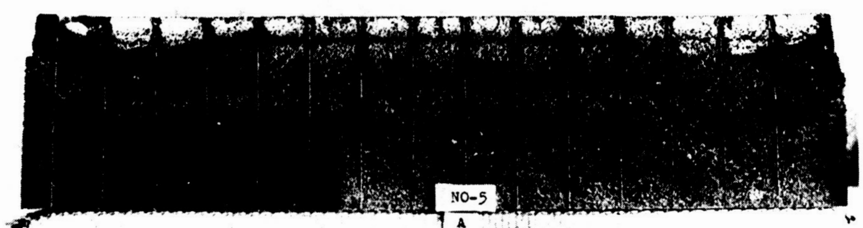

SLA-561
30-Pass Heating

Figure 30 - Cross-Section of Models After 30-Pass and 15-Pass Heating

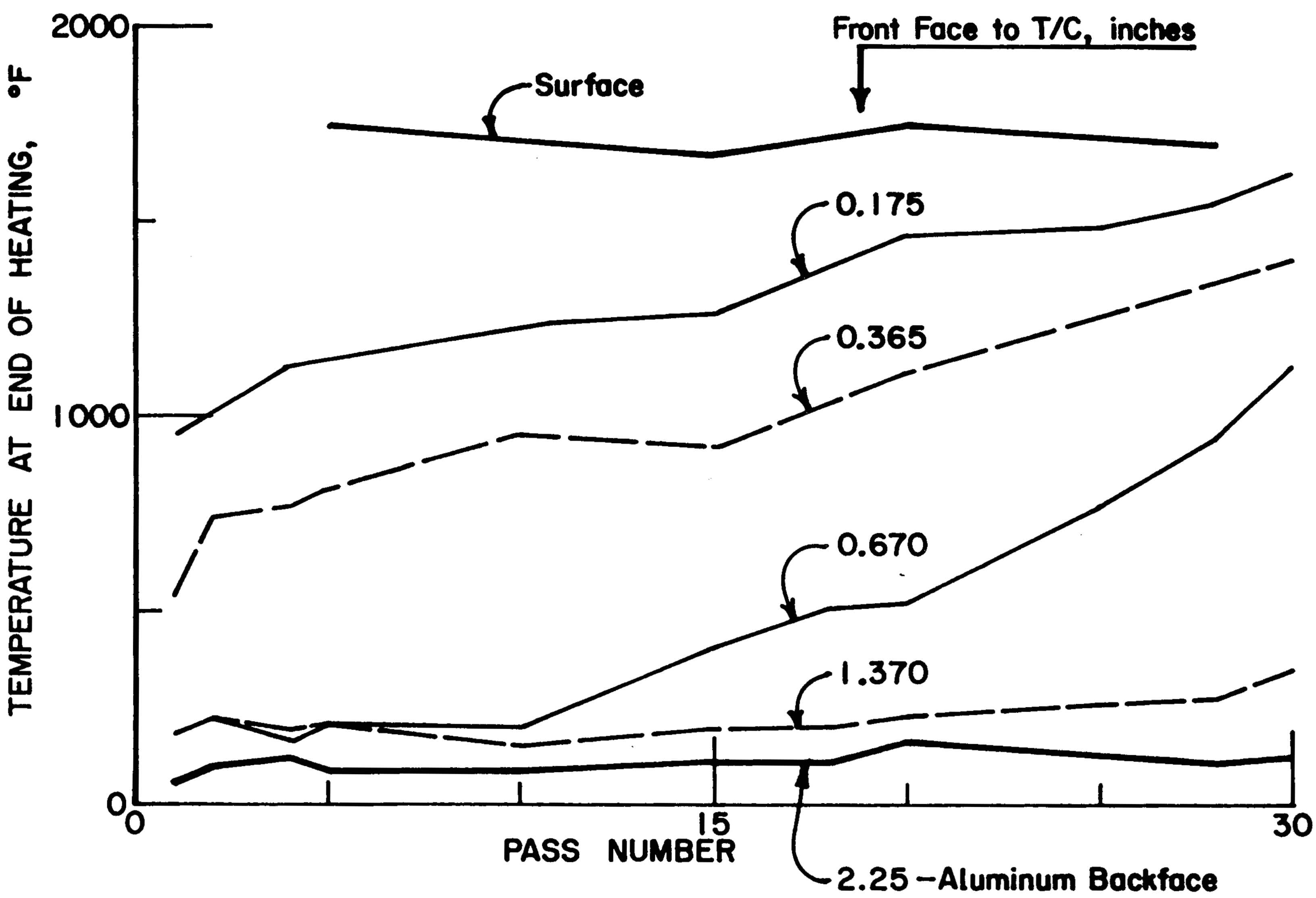

Figure 31 - Variation of Temperature at End of Heating with Entry Pass for ESA-3560, Model No. 1, 30-Pass Heating

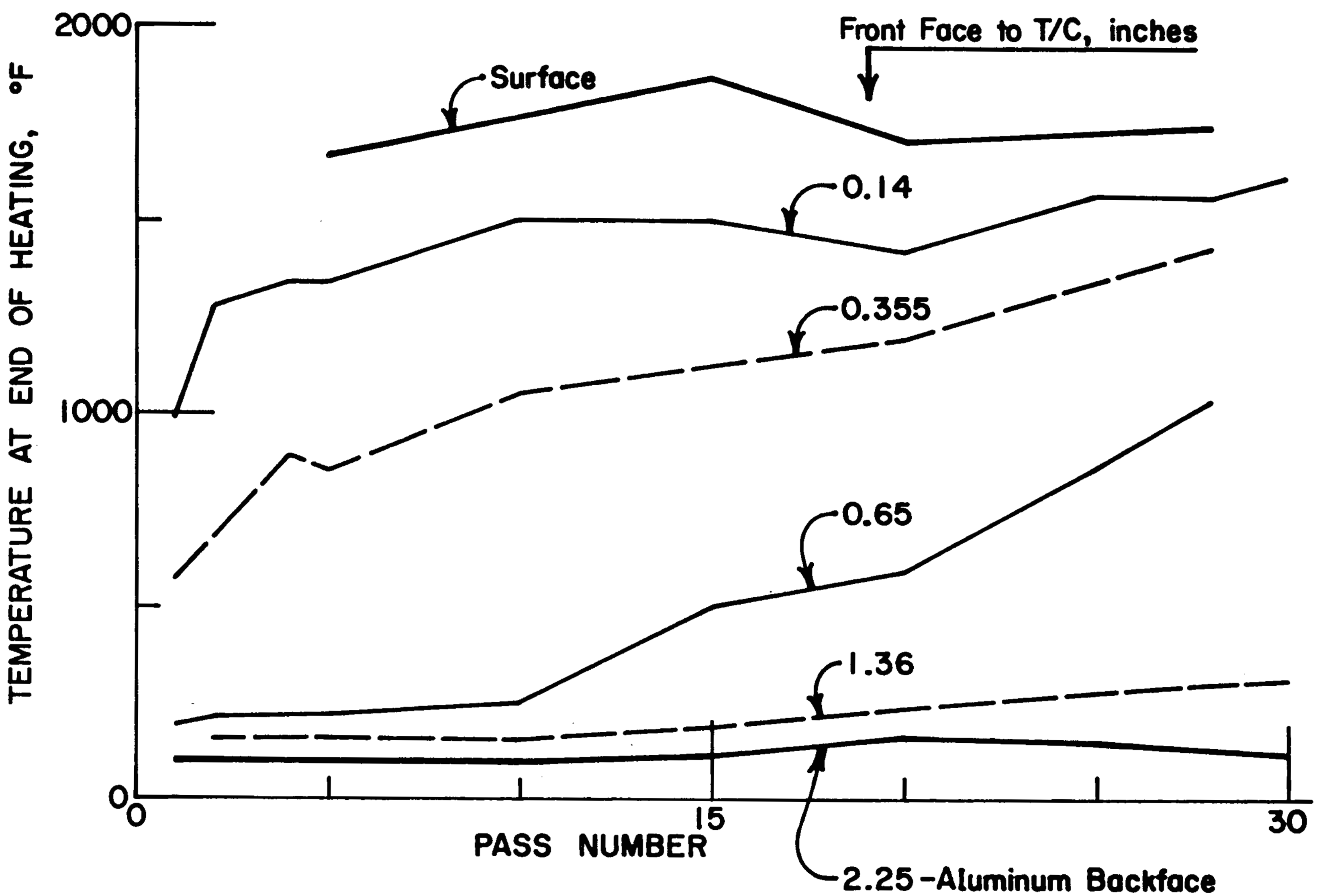

Figure 32 - Variation of Temperature at End of Heating with Entry Pass for ESA-3560, Model No. 2, 30-Pass Heating

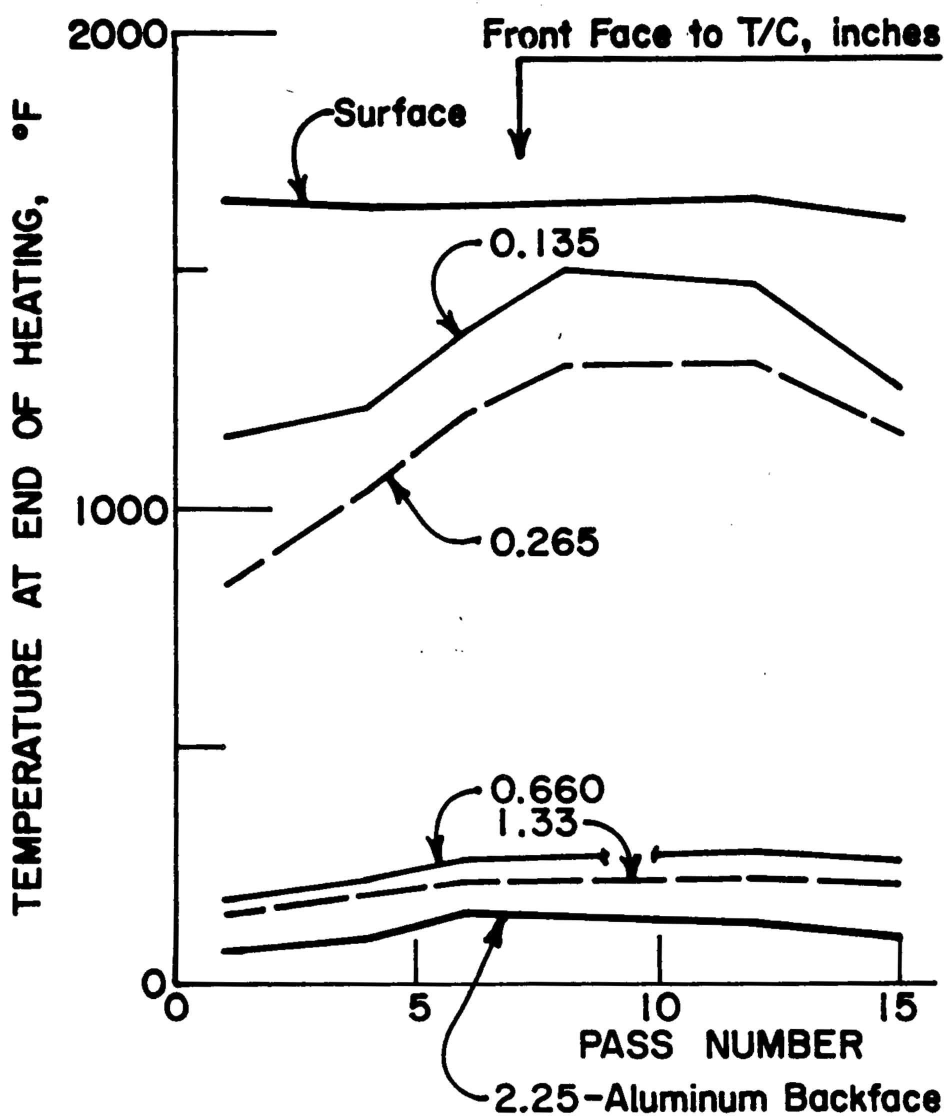

Figure 33 - Variation of Temperature at End of Heating with Entry Pass for ESA-3560, Model No. 3, 15-Pass Heating

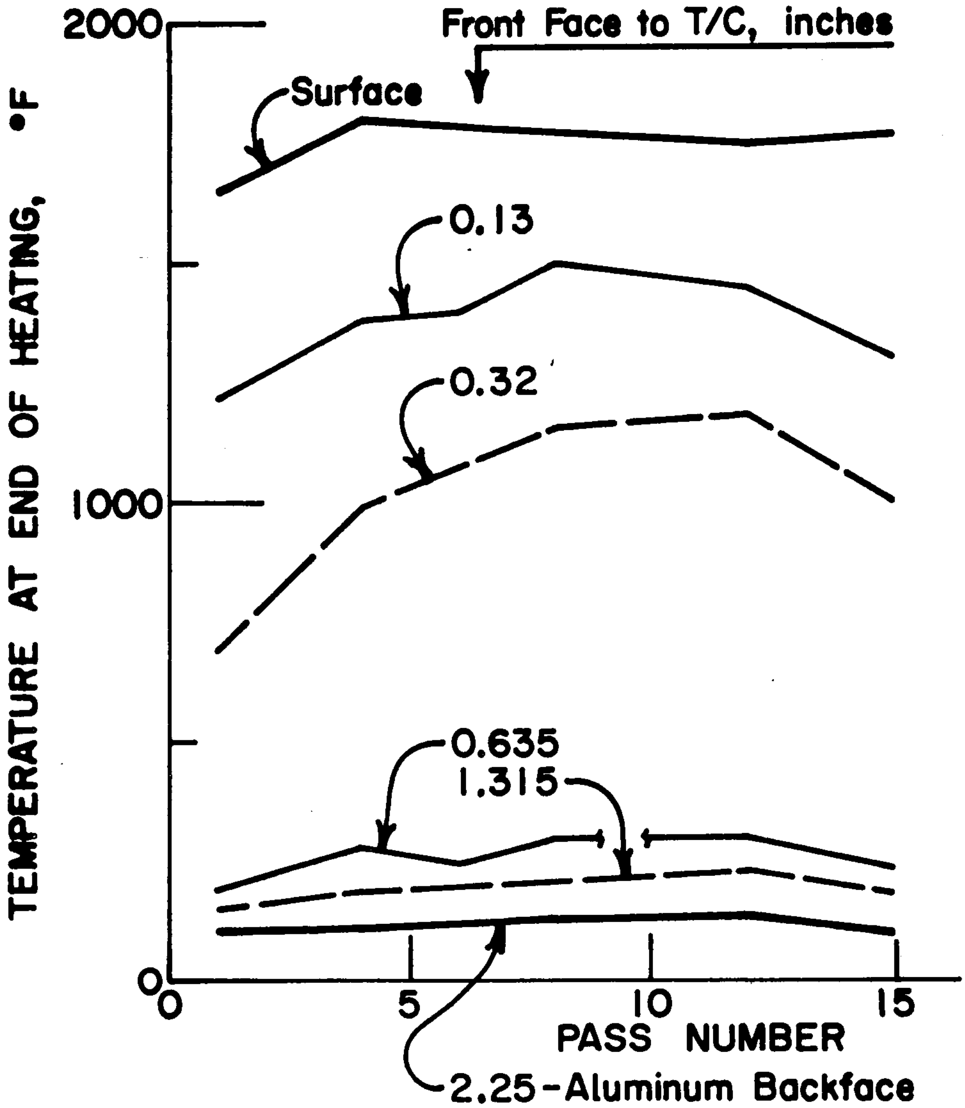

Figure 34 - Variation of Temperature at End of Heating with Entry Pass for ESA-3560, Model No. 4, 15-Pass Heating

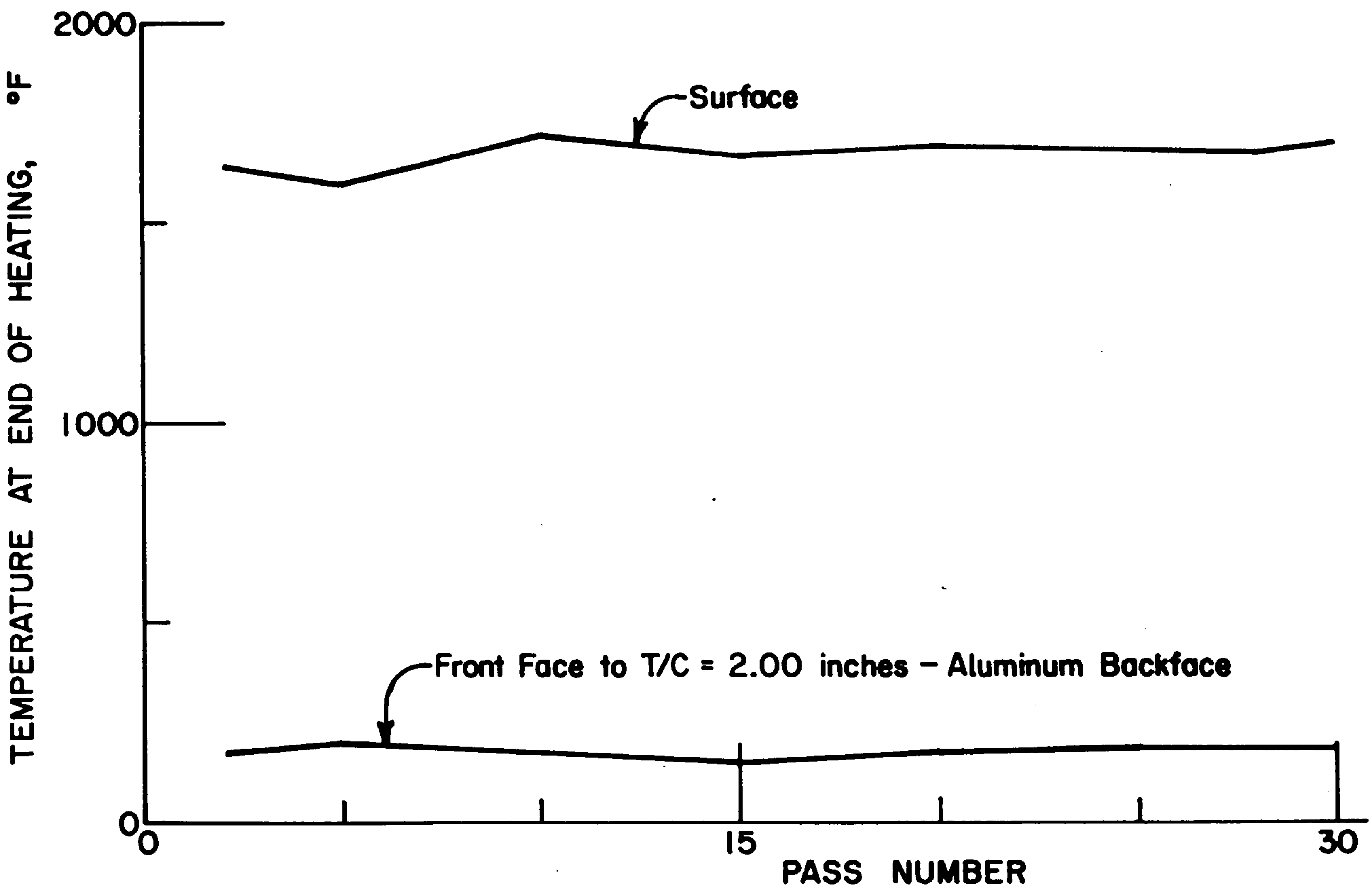

Figure 35 - Variation of Temperature at End of Heating with Entry Pass for SLA-561, Model No. 5, 30-Pass Heating

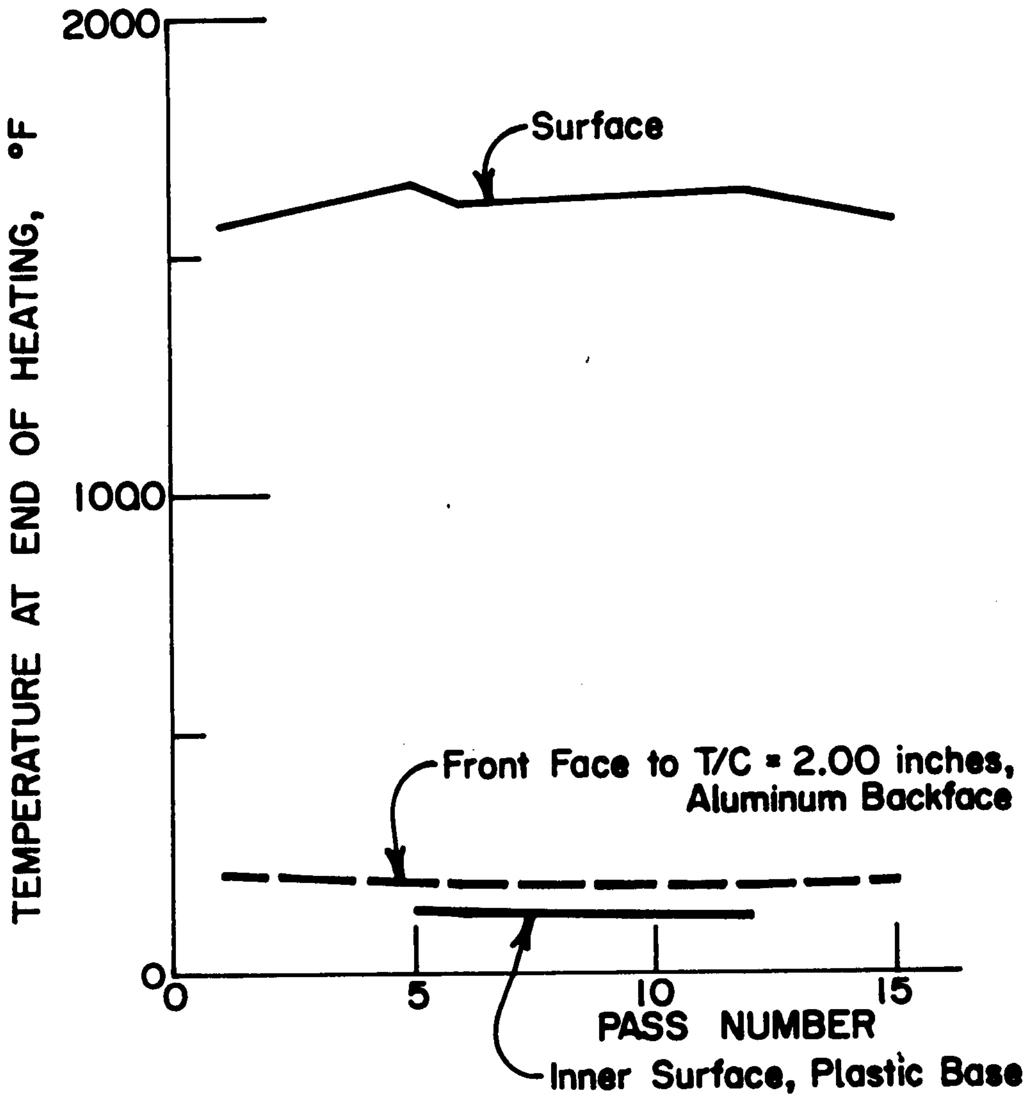

Figure 36 - Variation of Temperature at End of Heating with Entry Pass for SLA-561, Model No. 6, 15-Pass Heating

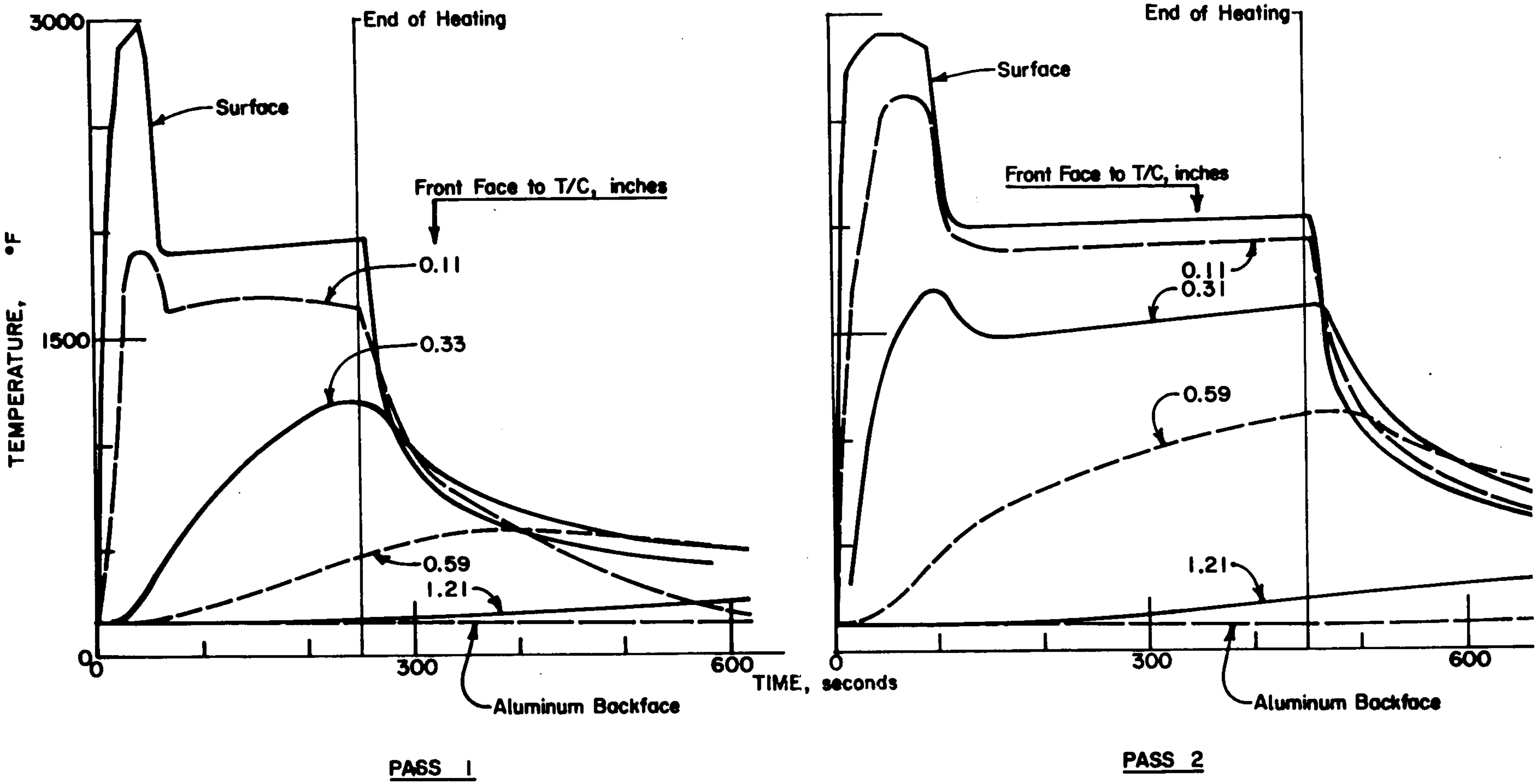

Figure 37 - Time-Temperature Traces for Analysis of ESA-5500 for Two-Pass Heating, Low Drag Configuration

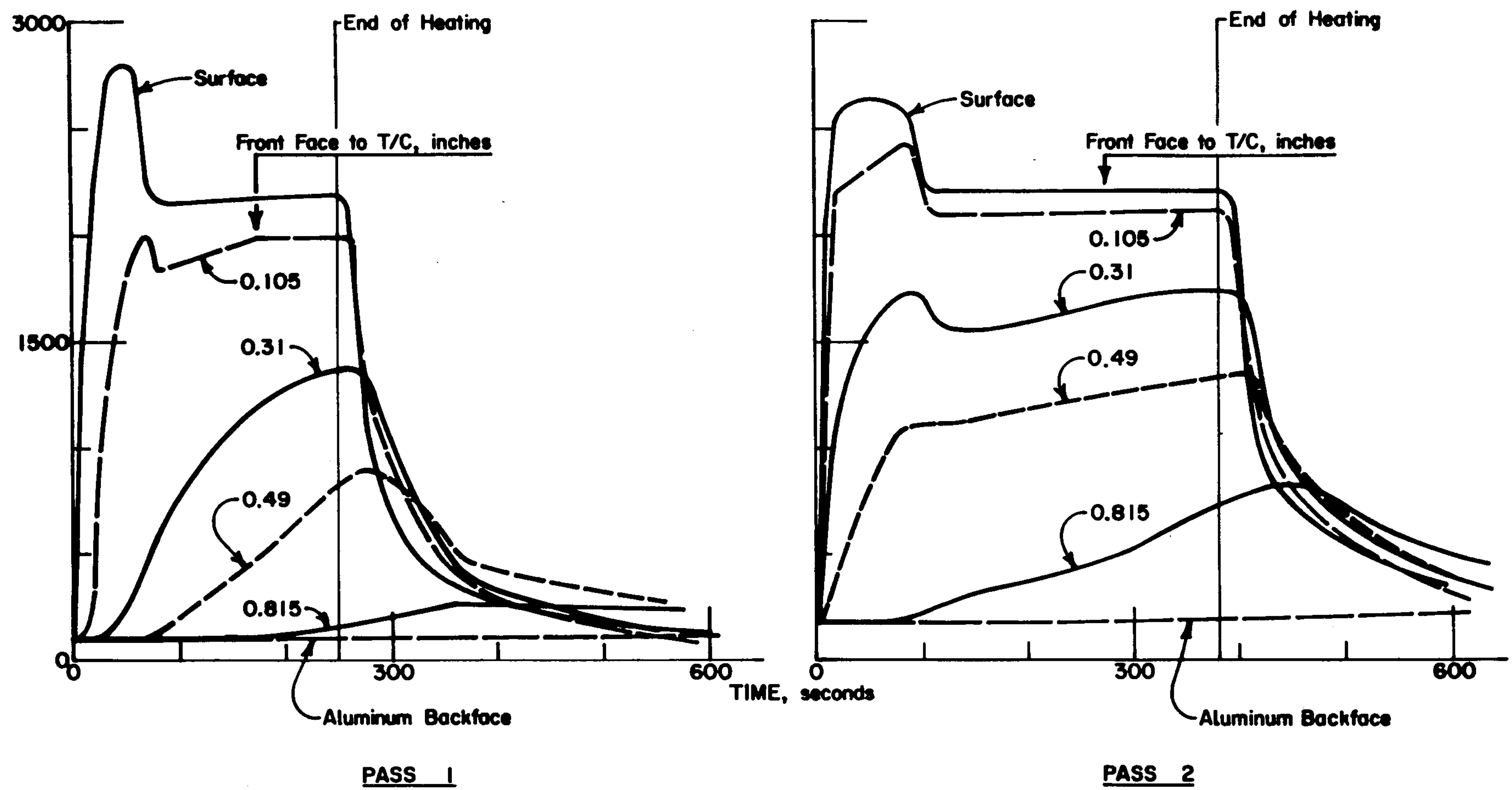

Figure 38 - Time-Temperature Traces for Analysis of ESA-3560 for Two-Pass Heating, High Drag Configuration

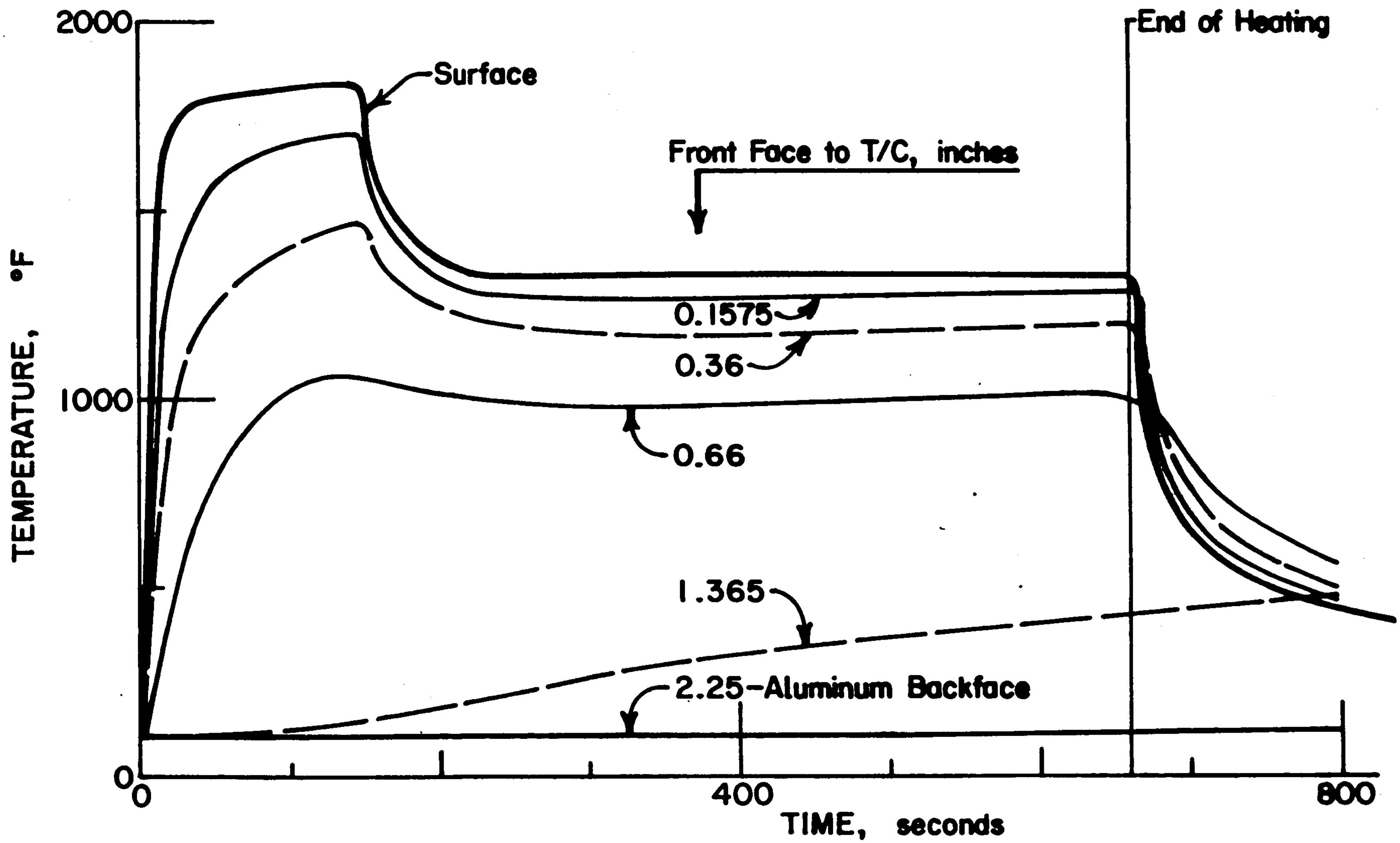

Figure 39 - Time-Temperature Traces for Analysis of ESA-3560 for Pass 30

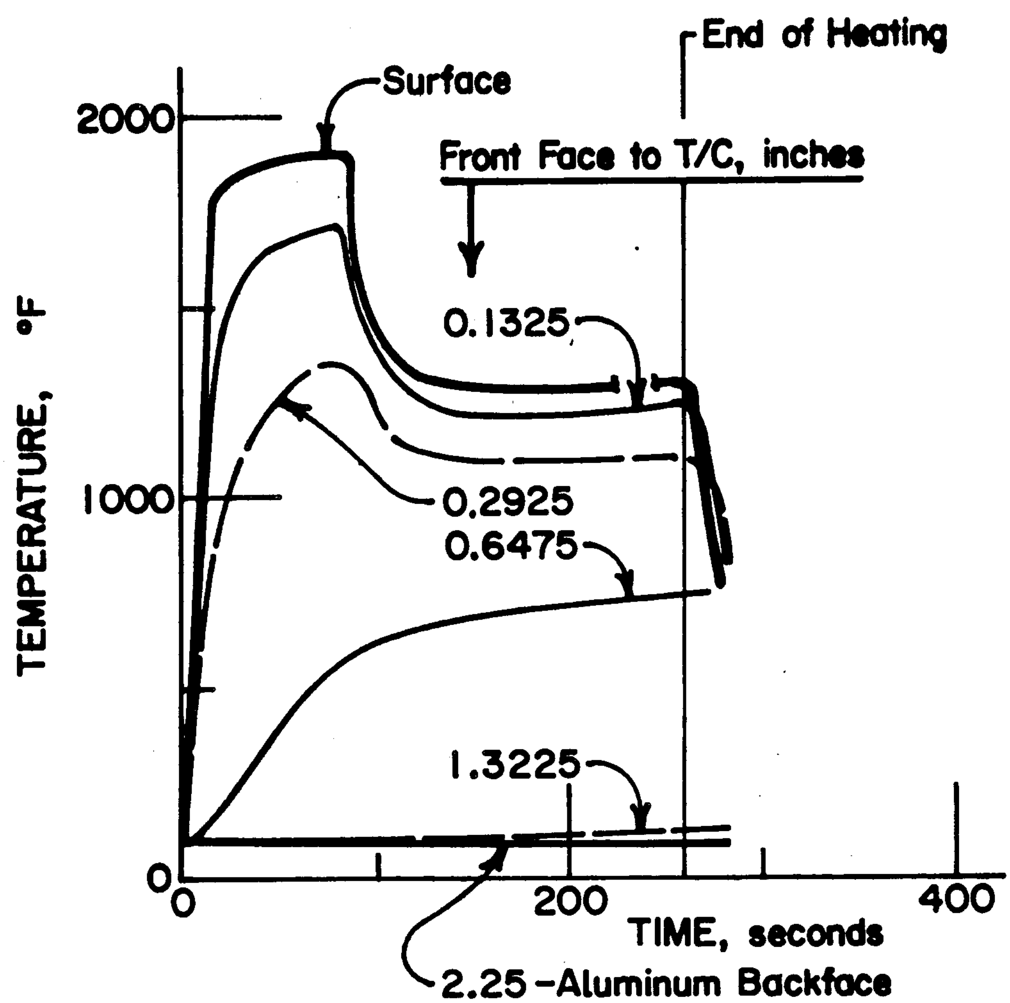

Figure 40 - Time-Temperature Traces for Analysis of ESA-3560 for Pass 15

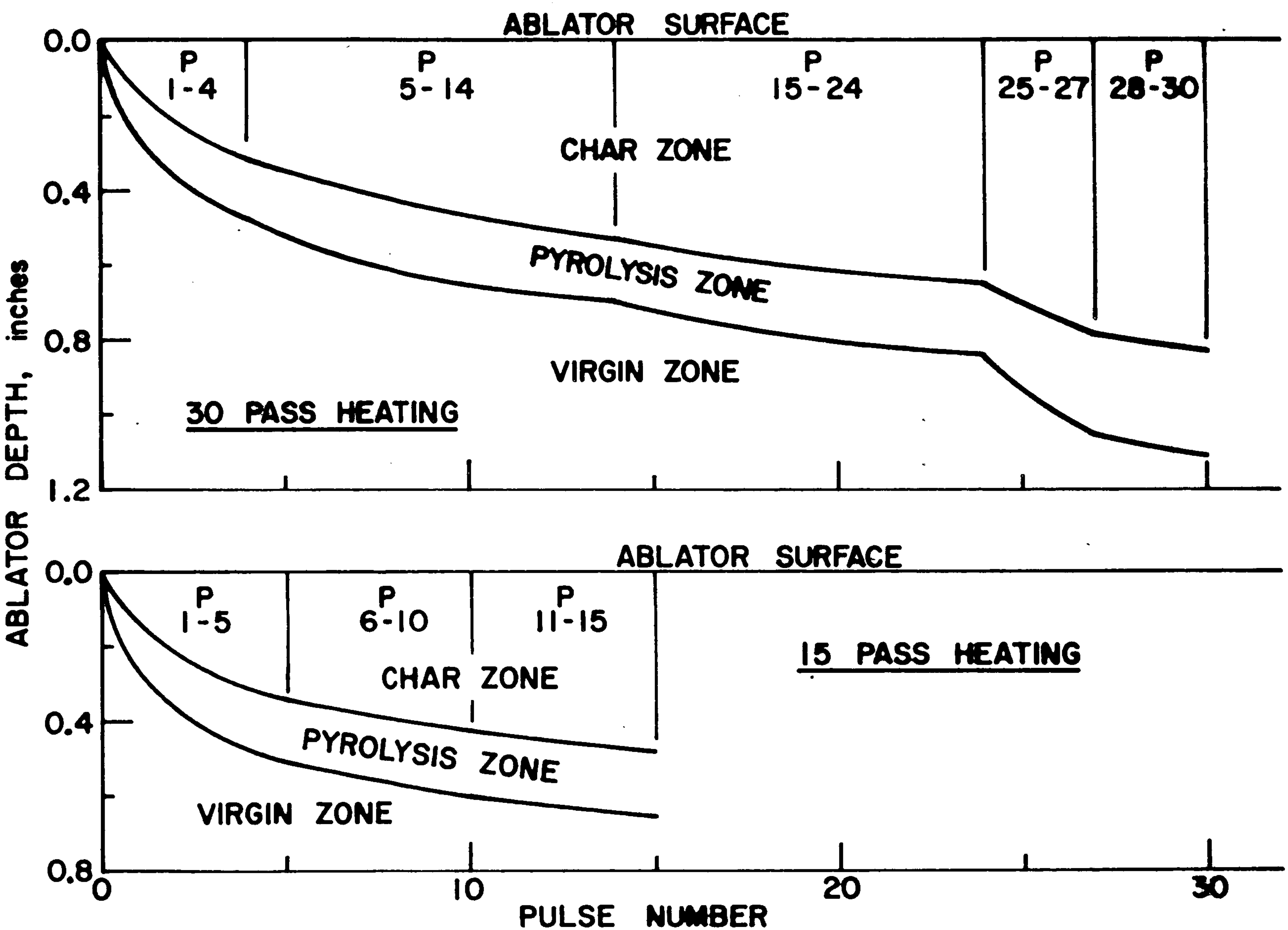

Figure 41 - Progression of Char Depth and Pyrolysis Zone During 30-Pass and 15-Pass Heating

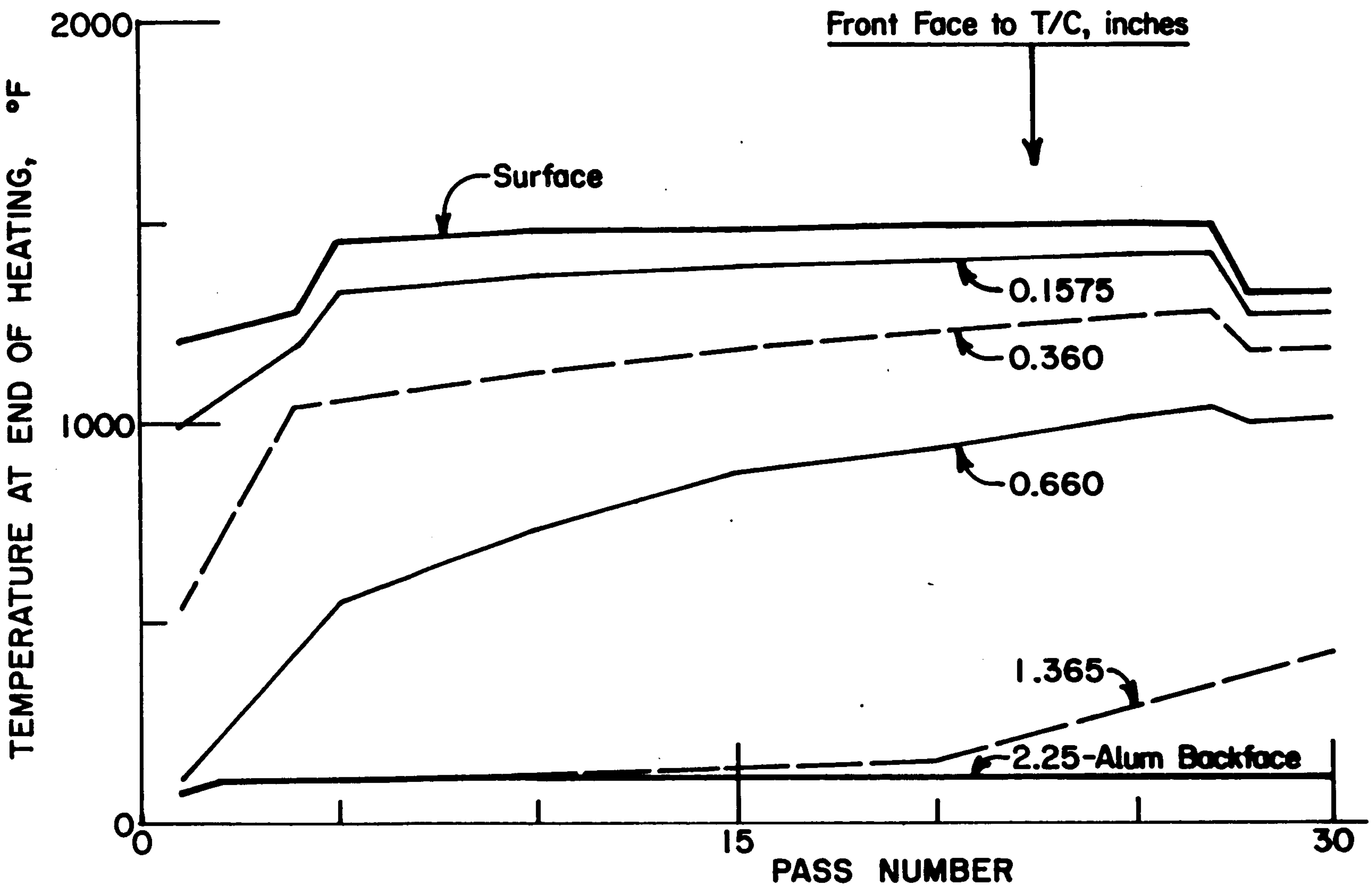

Figure 42 - Variation of Calculated Temperature at End of Heating with Entry Pass for ESA-3560, 30-Pass Heating

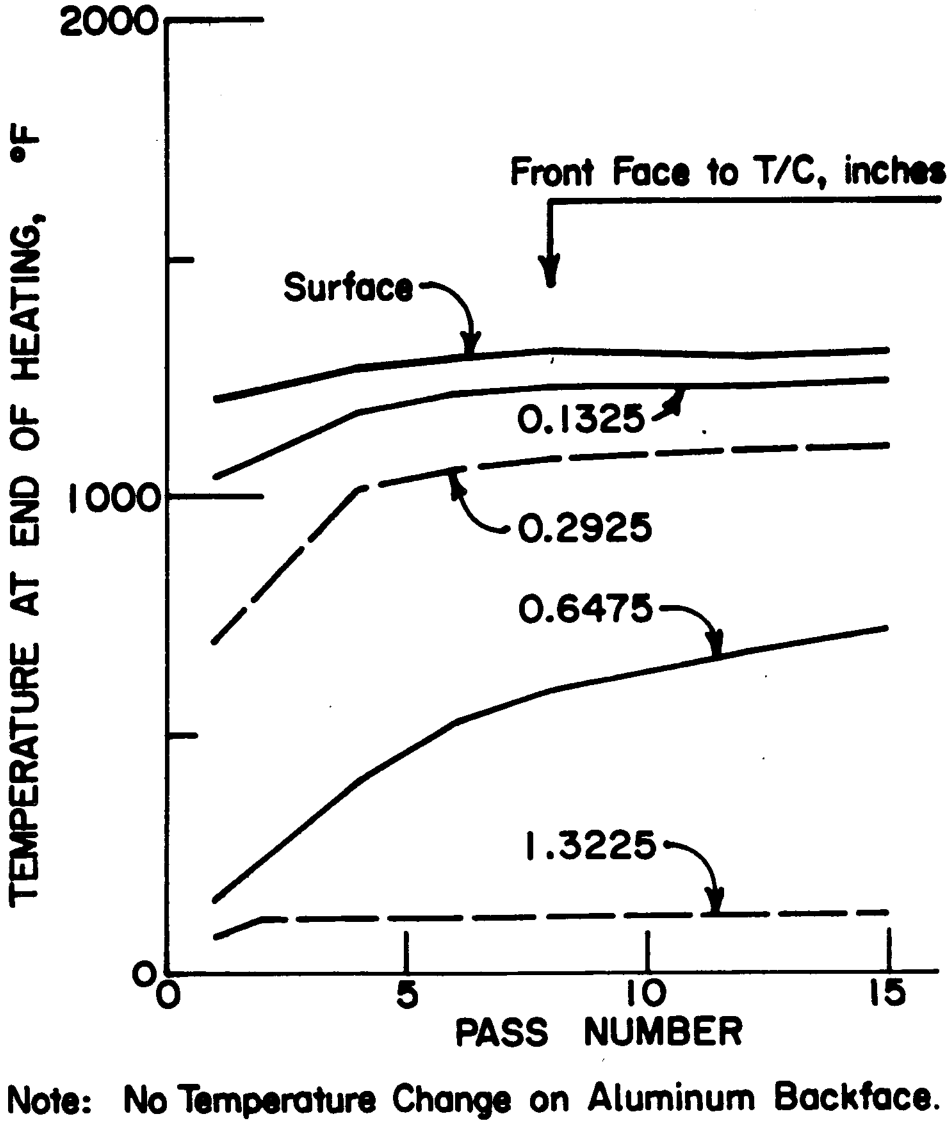

Figure 43 - Variation of Calculated Temperature at End of Heating with Entry Pass for ESA-3560, 15-Pass Heating

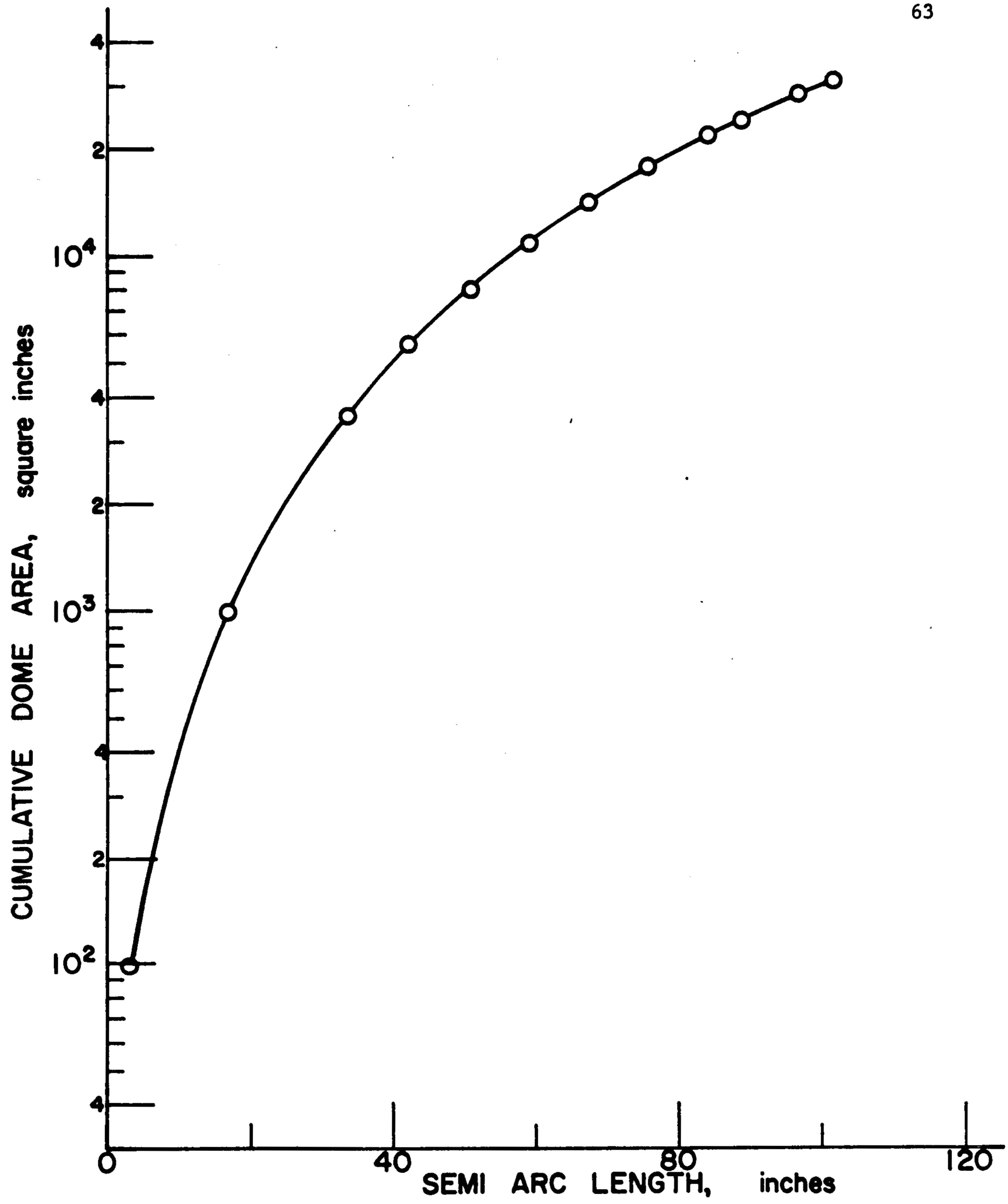

Figure 44 - Cumulative Dome Area for 2:1 Ellipse with a 84-inch Semi-Major Axis

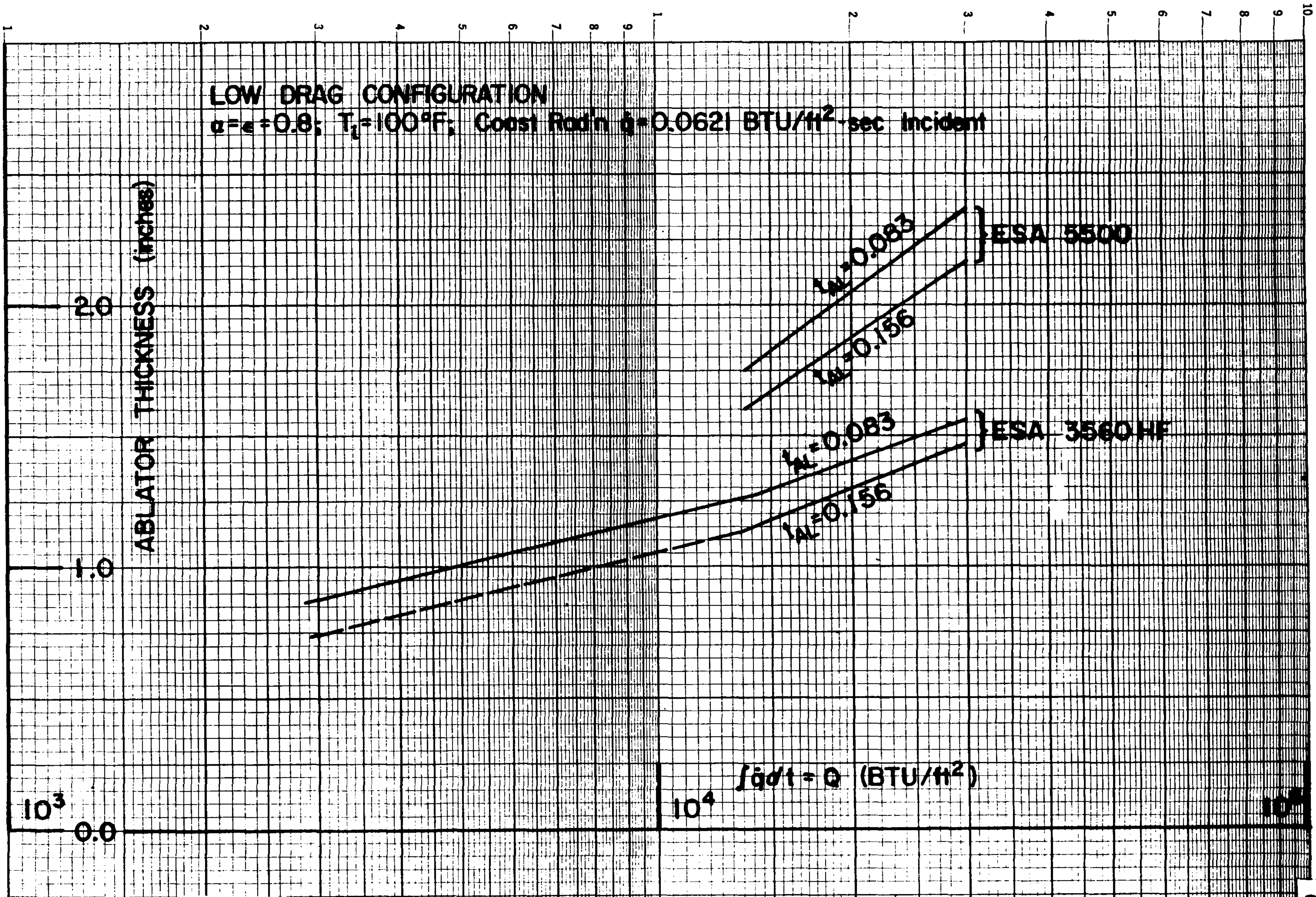

Figure 45 - Ablator Design Curves for Two-Pass Entry Missions (Supersedes Figure 26 of Reference 1)

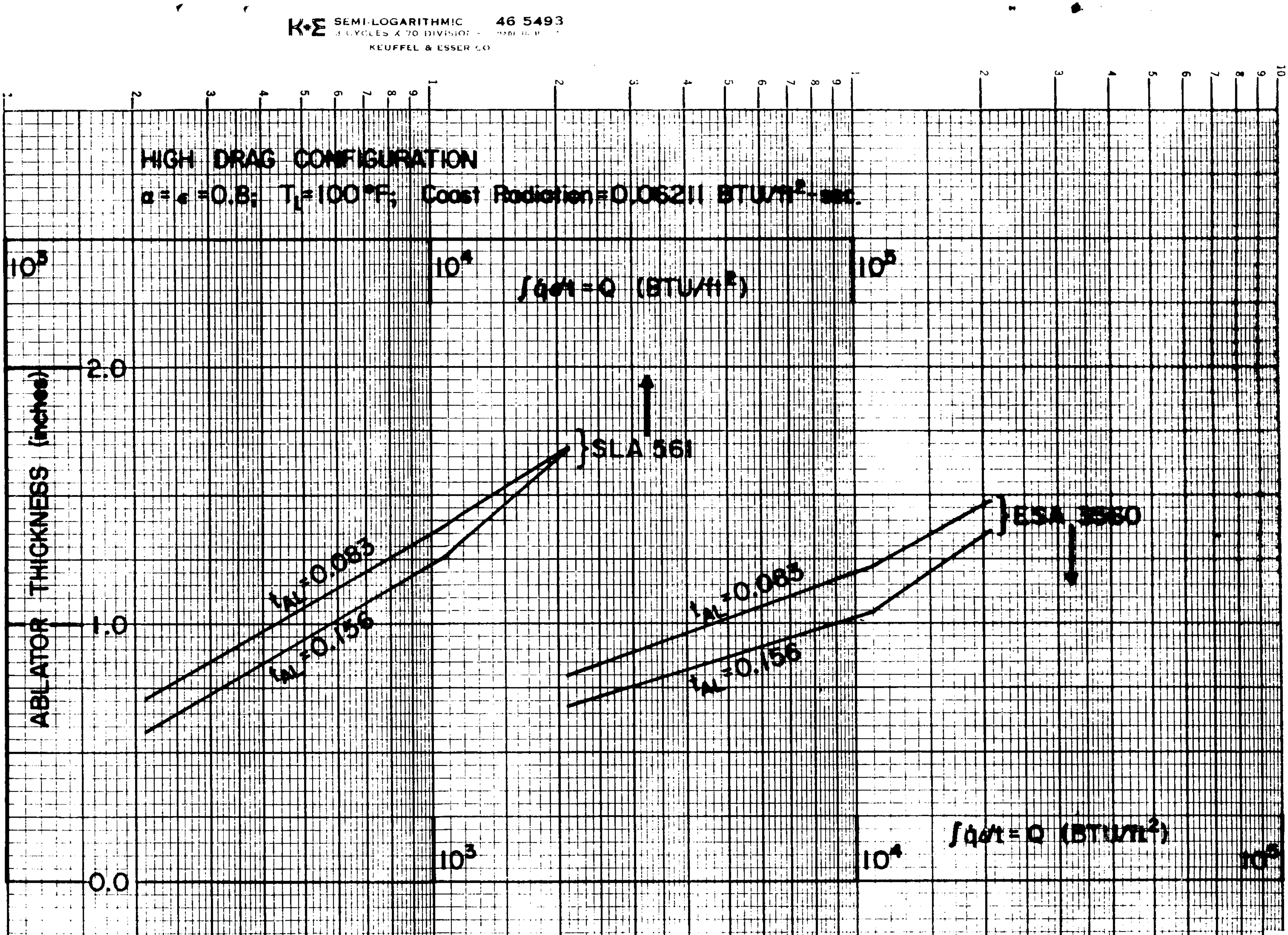

Figure 45 - Continued

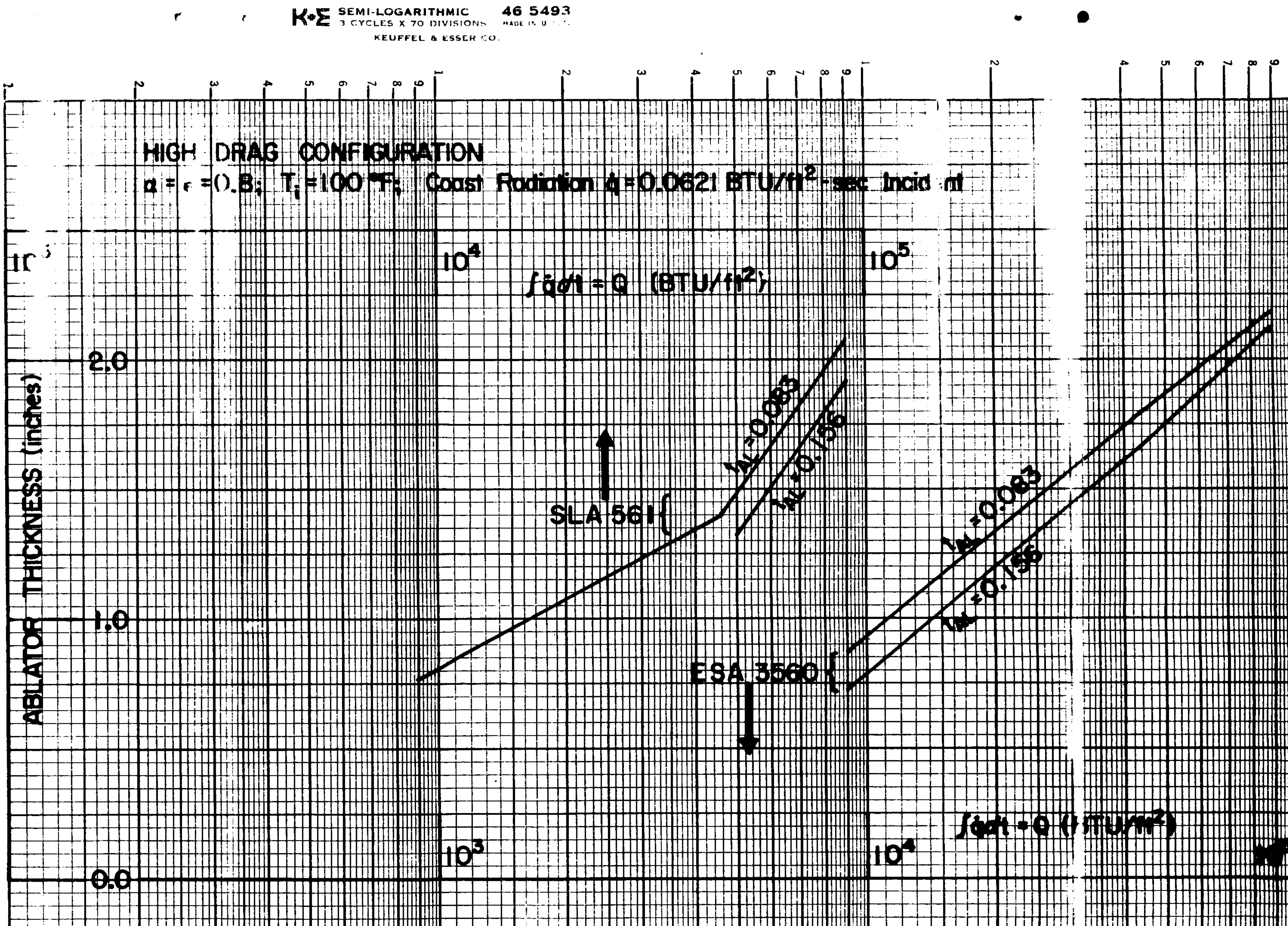

Figure 46 - Ablator Design Curves for Thirty-Pass Entry Missions (Supersedes Figure 27 of Reference 1)

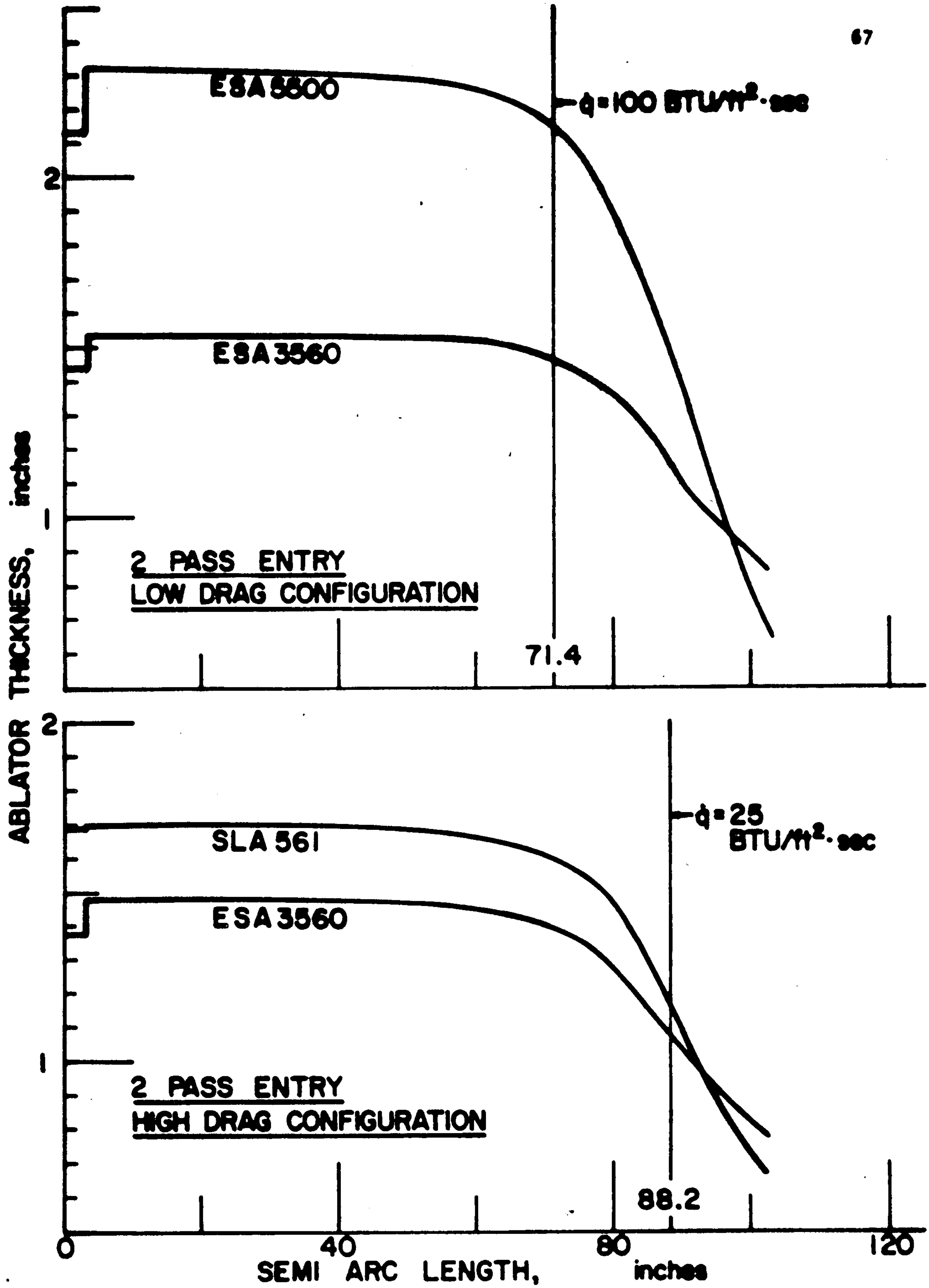

Figure 47 - Variation of Ablator Thickness with Location on the Elliptical Dome

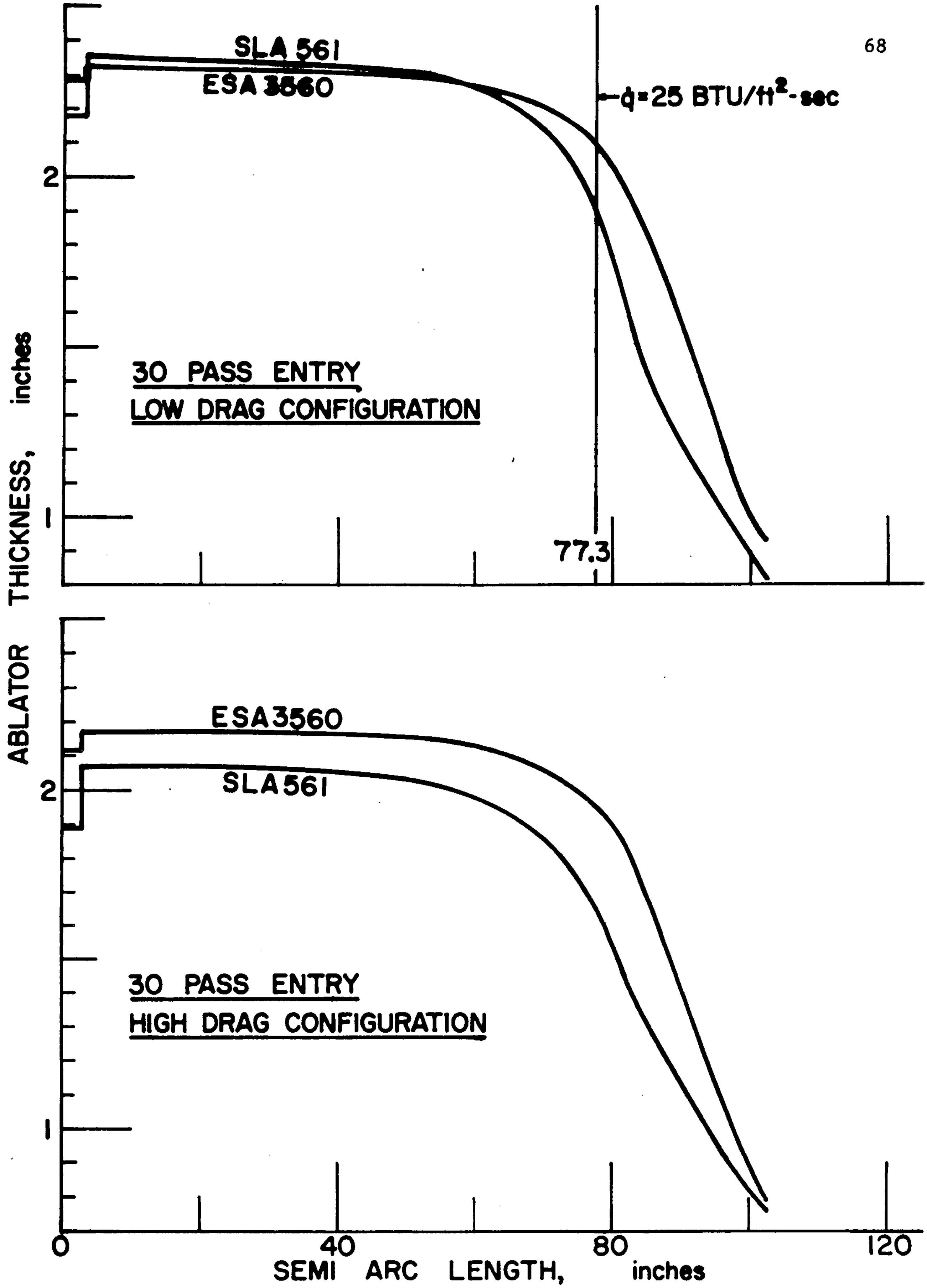

Figure 47 - Continued

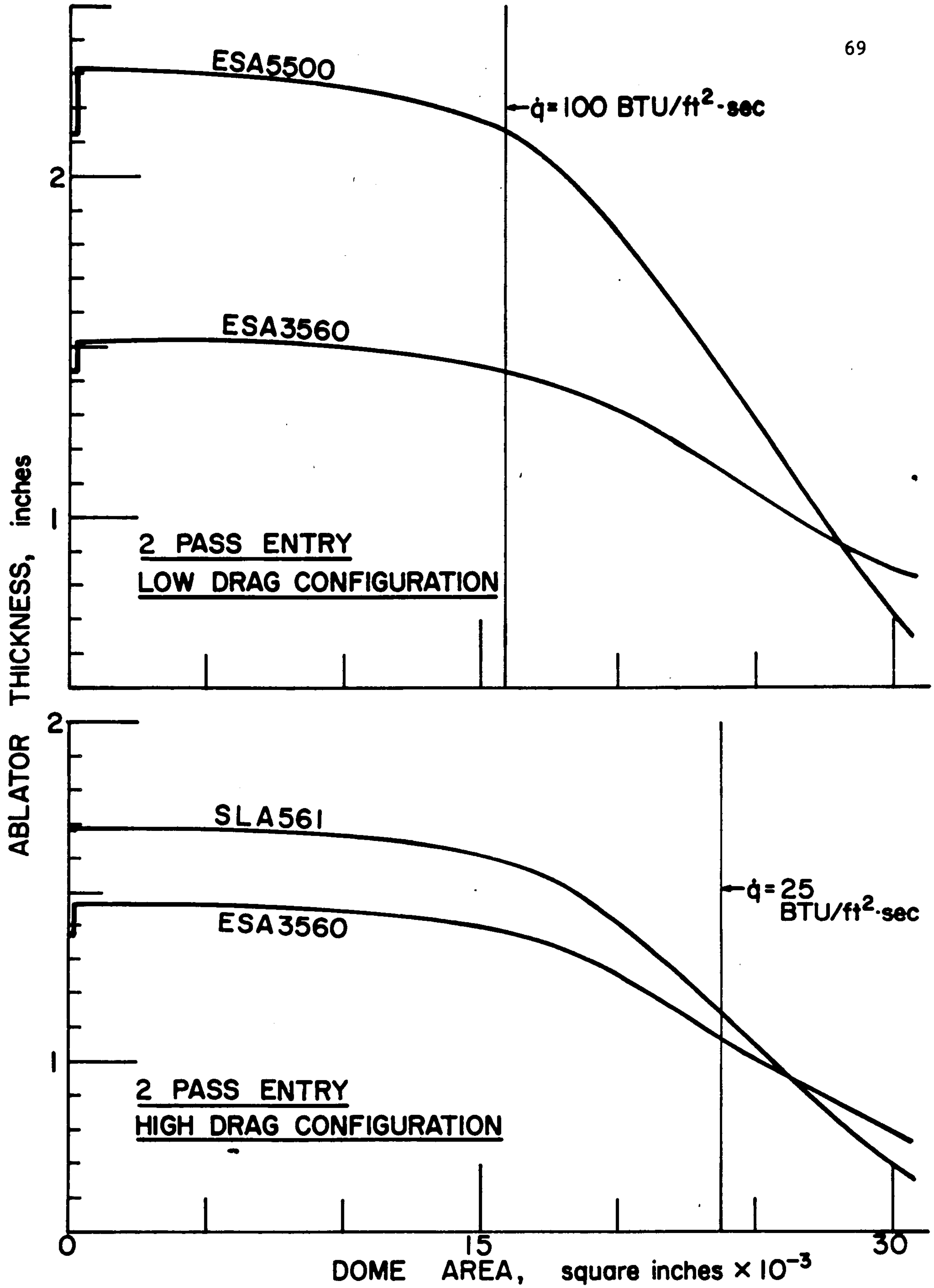

Figure 48 - Variation of Ablator Thickness with Dome Surface Area

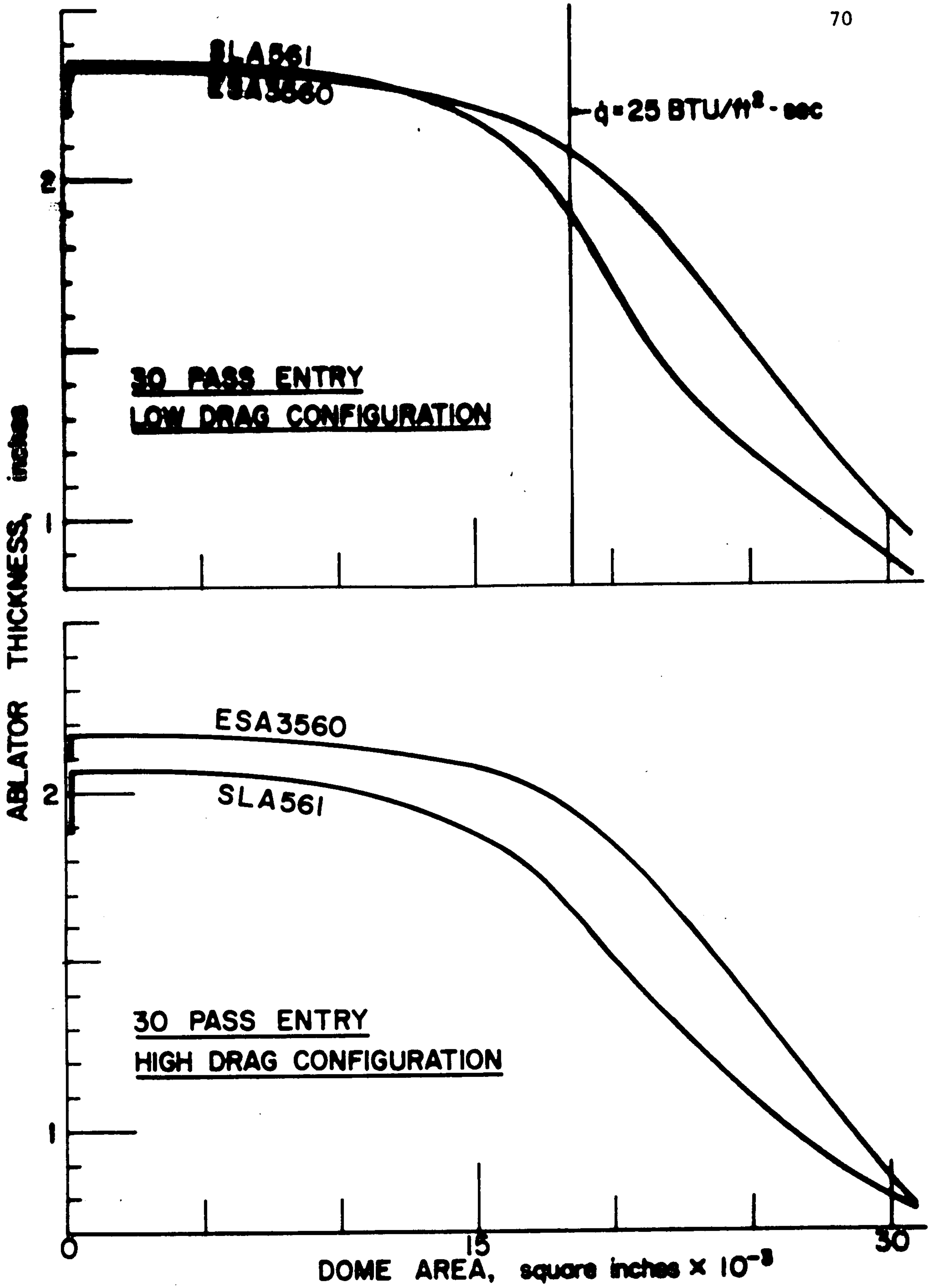

Figure 48 - Continued